

Rockwall permafrost dynamics evidenced by Repeated and Automated Electrical Resistivity Tomography at Aiguille du Midi (3842 m a.s.l., French Alps)

Feras Abdulsamad^{1,2}, Josué Bock¹, Florence Magnin¹, Emmanuel Malet¹, André Revil¹,
Matan Ben-Asher¹, Jessy Richard^{1,2}, Pierre-Allain Duvillard², Marios Karaoulis³, Thomas
Condom⁴, Ludovic Ravanel¹ and Philip Deline¹

1. EDYTEM, CNRS - Université Savoie Mont-Blanc, 73370 Le Bourget du Lac, France

2. Naga Geophysics, 229 rue Joseph Fontanet 73000 Chambéry, France

3. School of Geology, Geophysics Department, Aristotle University of Thessaloniki, Thessaloniki, Greece

4. Univ. Grenoble Alpes, IRD, CNRS, INRAE, Grenoble-INP, IGE, 38000 Grenoble, France

Corresponding author: Abdulsamad Feras (feras.abdul-samad@univ-smb.fr)

Emails: feras.abdul-samad@naga-geophysics.com; andre.revil@univ-smb.fr;
ludovic.ravanel@univ-smb.fr; florence.magnin@univ-smb.fr; mkaraoulis@geo.auth.gr;
matan.ben-asher@univ-smb.fr; pierre-allain.duvillard@naga-geophysics.com;
josue.bock@laposte.net; emmanuel.malet@univ-savoie.fr; jessy.richard@naga-geophysics.com;
thomas.condom@ird.fr; philip.deline@univ-smb.fr

Keywords: Rockwall permafrost dynamics; Active layer thickness; Electrical resistivity
tomography; Temperature measurements.

Intended for publication in The Cryosphere

26 **Abstract.** Permafrost degradation significantly affects the stability of rockwalls in high altitude
27 regions. Monitoring rockwall permafrost is essential for assessing potential geohazards. While
28 borehole temperature measurements are the most direct permafrost monitoring approach, they
29 lack sufficient spatial representation in such highly heterogeneous ground conditions.
30 Conversely, geoelectrical measurements can provide more comprehensive insights into these
31 complex patterns and dynamics. This study investigates the permafrost dynamics and intends
32 to detect potential hydrogeological processes at the Aiguille du Midi (3842 m a.s.l., French
33 Alps) using repeated and Automated-Electrical Resistivity Tomography (A-ERT) approaches,
34 covering a period of 3.5 years (06/2020-12/2023). A total of three geoelectrical profiles have
35 been installed on three faces of the Aiguille du Midi (N-W, S and E). An automated acquisition
36 system for permanent resistivity monitoring and remote data acquisition is implemented. A
37 time-lapse inversion technique is employed to get the temporal and spatial variations of
38 electrical resistivity at seasonal and interannual time scales. The data revealed significant
39 variations in active layer thickness across rock faces, along with a slight decrease in electrical
40 resistivity at depth, indicating permafrost warming over time. However, they did not provide
41 clear evidence of water pressurization in rock fractures. Using a petrophysical model, calibrated
42 with laboratory measurements of the temperature dependence of electrical resistivity of granite
43 sample, we estimated the temperature within the frozen zone from the resistivity measurements,
44 (under favorable condition at surface in summer and autumn). Validation against direct
45 temperature measurements in a 10-m depth borehole along the NW profile indicates a mean
46 absolute error demonstrates an accuracy of less than approximately ± 1 °C within the frozen
47 zone. This research underscores the efficacy of ERT as a promising, non-invasive tool for
48 quantitative monitoring of permafrost dynamics in Alpine environments. It also reveals
49 challenges associated with conducting A-ERT in high mountain rockwalls where the contact

50 resistance is very high ($\sim 500 \text{ k}\Omega$) and sometimes intermittent due to factors such as thunder
51 strikes and rockfalls.

52 **1. Introduction**

53 Climate change accelerates the degradation of the permafrost in high-mountains areas
54 worldwide (Smith et al., 2022). In the European Alps, permafrost has warmed up to $> 1^\circ\text{C}$ at
55 10 m depth, especially in bedrock permafrost (Etzelmüller et al., 2020; Magnin et al., 2024;
56 Noetzli et al., 2024). Over the last decade, there has been a continuous increase in rockfall
57 events, particularly those impacting permafrost in the European Alps (Cathala et al., 2024;
58 Jacquemart et al., 2024; Ravanel et al., 2017). Infrastructure located in high altitude are
59 increasingly affected by these events (Duvillard et al., 2021, 2018; Hartmeyer et al. 2020).
60 Permafrost degradation of the rock mass can also locally be accelerated by heat advection
61 through water infiltration in fractures (see for example Hasler et al., (2011) for a laboratory
62 experiment; Magnin and Josnin (2021) for a numerical experiment), leading to erosion of the
63 ice-infill (Hauck and Hilbich, 2024; Hartmeyer et al. 2020). As a result, a loss of bonding
64 between rock and ice may occur, which in turn alters the mechanical properties of such
65 assemblage (Mamot et al., 2018; Krautblatter et al., 2013). Therefore, understanding the
66 thermo-hydrogeological dynamics of steep Alpine rock faces is essential for assessing potential
67 geohazards associated with permafrost degradation.

68 To assess permafrost warming, one approach is to directly determine and monitor
69 rockwall temperatures using temperature sensors installed at the rock surface or in boreholes
70 (*e.g.*, Magnin et al., 2024). Although borehole temperature monitoring is still the only direct
71 method to detect and monitor permafrost, it provides only point-scale information, while its
72 distribution and evolution can be highly variable in extreme topographical conditions. In
73 addition, boreholes in rockwall at high altitude are logistically difficult to realize. and are also
74 expensive and invasive.

75 On the other hand, geophysical measurements provide higher spatial coverage with
76 respect to boreholes. Various non- or minimally intrusive methods have been applied to
77 evaluate permafrost, including Refraction Seismic Tomography (RST) (*e.g.*, Steiner et al.,
78 2019; Draebing 2016), Ground Penetrating Radar (GPR) (Campbell et al., 2018), Electrical
79 Resistivity Tomography (ERT) (*e.g.*, Mollaret et al., 2020; Krautblatter and Hauck 2007) and
80 Induced Polarization (IP) (Maierhofer et al., 2024; Abdulsamad et al., 2019; Duvillard et al.,
81 2018; Doetsch et al., 2015). Combined geophysical methods can take advantage of the
82 complementary petrophysical and spatial sensitivities of these different methods. For instance,
83 ERT measurement was combined with RST to evaluate ice, air, water, and rock contents
84 (Mewes et al., 2017; Hauck et al., 2011). Recently, joint inversion of ERT and RST could
85 reduce the uncertainties in the evaluation of air, water, ice and rock contents (Pavoni et al.,
86 2023; Steiner et al., 2021; Mollaret et al., 2020; Wagner et al., 2019). IP measurements
87 (providing tomograms of the electrical conductivity and normalized chargeability) have been
88 recently used to assess the distribution of permafrost temperature, relying on laboratory
89 calibration and a petrophysical (physics-based) model connecting resistivity and normalized
90 chargeability with temperature under frozen and unfrozen conditions (see Moser et al., 2025;
91 Duvillard et al., 2021, 2018; [Revil et al. 2026a, b](#) and references therein).

92 In the last two decades, ERT has become an increasingly popular tool in permafrost
93 studies (*e.g.*, Herring et al., 2023; Farzamain et al., 2020; Magnin et al., 2015a; Krautblatter et
94 al., 2010). Herring et al. (2023) provide a review of the use of ERT method in permafrost
95 research, detailing both the advantages and limitations of this method in such a context. A
96 significant advantage of using electrical resistivity measurements to assess mountain
97 permafrost is that the freezing and thawing of water filling pores are associated with
98 considerable changes in resistivity (generally between one to three orders of magnitude, see

99 Coperey et al., 2019). Because of this sensitivity, electrical resistivity tomograms can be used
100 to assess the presence and distribution of permafrost.

101 Repeated ERT measurements at specific time intervals using the same survey geometry
102 can be used to track the temporal and spatial evolution of permafrost over time (*e.g.*, Offer et
103 al., 2025, Hilbich et al., 2008). However, rapid changes due to water flow, infiltration or
104 drainage (such as during snowmelt or rainfall) may not be captured by monthly or seasonally
105 repeated measurements (Krautblatter et al., 2010). Alternatively, continuous resistivity
106 measurements, known as Automated-ERT (A-ERT) or ERT monitoring, offer the ability to
107 track the ongoing evolution of permafrost and capture rapid, heterogeneous and non-linear
108 changes in its temperature and ice content (*e.g.*, Scandroglio et al., 2021; Doetsch et al., 2015).
109 A-ERT over period of several years has been recently used to track the degradation of
110 permafrost associated with global warming (Mollaret et al., 2019; Keusching et al., 2017;
111 Doetsch et al., 2015; Hilbich et al., 2008).

112 Furthermore, the time-lapse inversion of geophysical data derived from a fixed
113 monitoring network provides a succession of tomograms showing the spatial and temporal
114 changes in subsurface resistivity (see; Karaoulis et al., 2013; Loke, 1999). The results of time-
115 lapse inversions of apparent resistivity data can be directly linked to the evolution of permafrost
116 throughout the annual cycle or to rapid variations caused by water infiltration or drainage during
117 short periods of time (Cimpoiasu et al., 2025; Keusching et al., 2017; Hilbich et al., 2008).

118 That said, A-ERT at high altitudes (>3500 m) and over a multi-profile setting has not
119 yet been tested for pluriannual permafrost monitoring. The use of A-ERT under high-altitude
120 conditions presents specific challenges due to extreme topographical and climatic conditions as
121 well as meteorological events. However, it could provide valuable information about the
122 hydrogeological system and the evolution of permafrost in environments where its distribution
123 and dynamic are highly heterogeneous.

124 In this study, we present the results of an A-ERT survey conducted over nearly four
125 years (2020-2023) at Aiguille du Midi (AdM) in the Mont-Blanc massif (French Alps). The site
126 consists of massive and fractured granite and includes infrastructure such as tunnels and
127 elevators. Water infiltration was observed at various locations within the tunnels. The objective
128 of this study is to investigate permafrost dynamics from infra-seasonal to multiyear timescales
129 and through various rock faces of the same site. Our goals are: (1) evaluating the potential of
130 A-ERT to characterize seasonal to pluriannual permafrost dynamics, their heterogeneity and
131 non-linearity in steep alpine rockwalls; (2) assessing the accuracy of temperature derived from
132 resistivity measurements; and (3) attempting to detect potential water circulation pathways- in
133 fractures, along with their thermal impacts. For this objective, a total of three ERT profiles were
134 deployed downwards from the summit in three directions: North-West (NW), South (S) and
135 East (E). Each profile consists of 32 electrodes spaced at 5 m. In addition to field data,
136 laboratory resistivity measurements were conducted on granite core samples, in both unfrozen
137 and frozen conditions. Furthermore, temperature was continuously monitored in a 10 m-deep
138 borehole along the NW profile and was used to quantitatively evaluate the accuracy of
139 temperature estimates derived from geophysical measurements of electrical resistivity.

140 **2. Study site**

141 We investigate the Aiguille du Midi (3842 m a.s.l.), which is the highest and most
142 western summit of the Aiguilles de Chamonix (Fig. 1a). It is located on the NW flank of the
143 Mont-Blanc massif. It includes three peaks that are all connected by human-made bridges and
144 galleries and hosts major touristic and technical infrastructures. During the summer season,
145 AdM is visited by approximately 5000 visitors per day, who are transported from the city of
146 Chamonix by cable car, making it one of the most intensively frequented high-alpine sites in
147 the European Alps. Since the 1950s, the morphology and appearance of the summit have been
148 strongly modified by construction and infrastructure development (Fig. 1). These factors,

149 combined with the extreme topography characterized by near-vertical rock walls with an
150 average slope of 78° on the northwestern face, make the site particularly prone to rock
151 instability processes. Consequently, AdM represents a critical location where geotechnical and
152 geophysical monitoring is essential to ensure the long-term stability of the infrastructures and
153 the safety of visitors. Our study focuses on the central peak, which is the highest among the
154 three, and which hosts the cable-car station connecting AdM to Pointe Helbronner with the
155 *Panoramic Mont-Blanc* cable car.

156 The lithology in the study area is dominated by massive granite with a very low porosity
157 (~ 0.01 , Magnin et al., 2015a). The highest parts (3740 to 3840 m a.s.l.) of the peak tend to be
158 steep, contain few large fractures, and, in places, are characterized by vertical foliation bands
159 and small cracks (Magnin et al., 2015b). Figure 2 shows the mean monthly and annual air
160 temperature at AdM during the study period. The year 2021 was the coolest year (yearly
161 averages: -5.8°C , -6.9°C , -5.3°C , and -5.7°C from 2020 to 2023, respectively), and 2022 was
162 the warmest especially due to extremely warm summer that had important consequences on
163 rock temperature (Magnin et al., 2024; Bruel et al., 2026).

164 In order to evaluate the thermal state and the distribution of permafrost at AdM, three
165 boreholes have been drilled in 2009. They are labeled BH-NW on the NW face, BH-S on the
166 South face and BH-E on the East face. Each borehole is 10-m-deep and 66 mm in diameter and
167 was drilled normal to the topography (their position is shown in Fig. 1b-d). Each borehole is
168 equipped with 15-thermistor strings calibrated in an ice-water bath and then placed at different
169 depths in the borehole. Figure A1 shows the temperature measured in BH-NW and BH-S at
170 different dates.

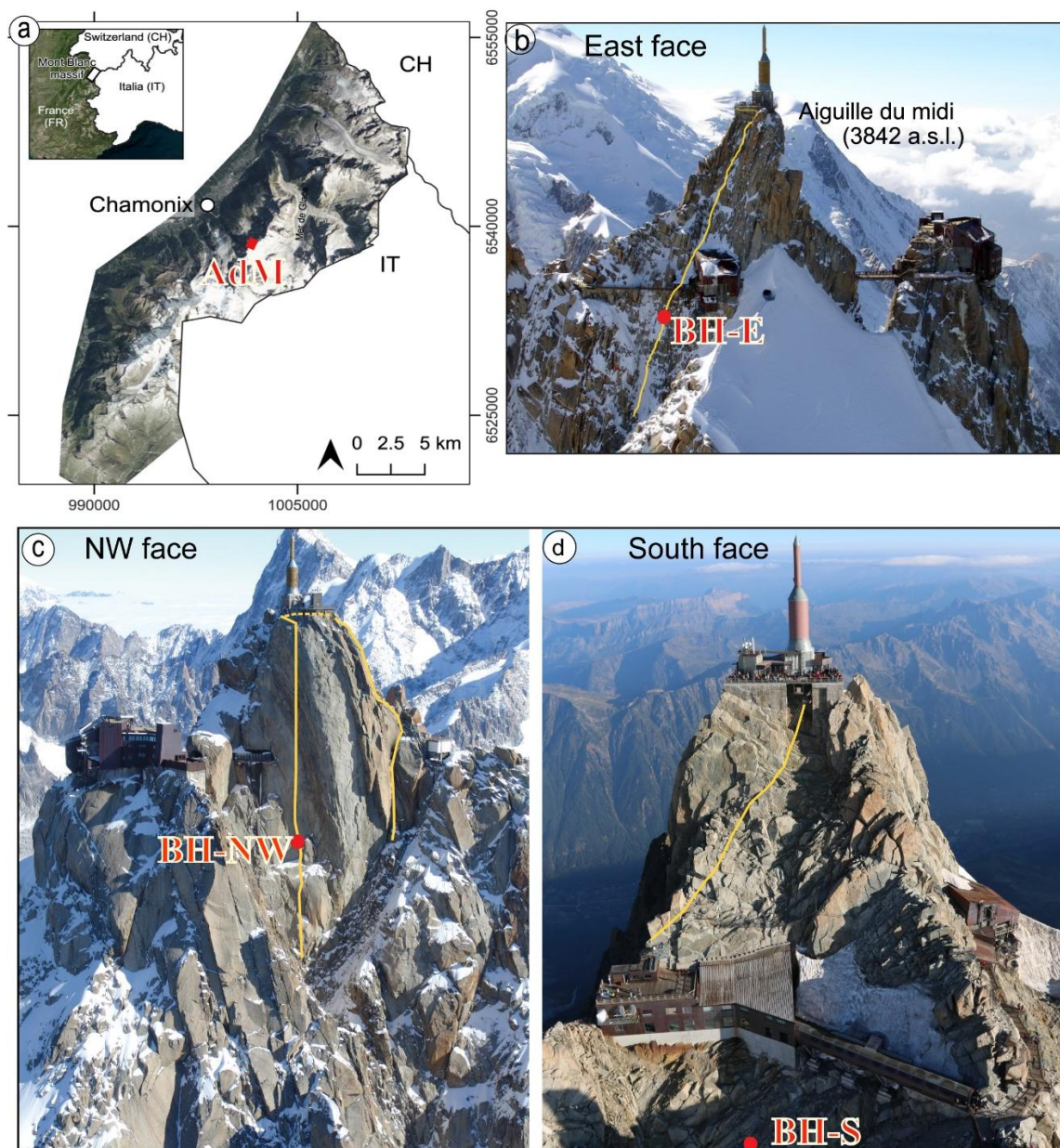
171 The temperature of the permafrost core shows significant variability between the South
172 and North-West faces of the AdM. For example, at a depth of 10 meters, the temperature is
173 approximately -4°C on the NW face, while it is around -1°C on the sun-exposed S face

174 (Magnin et al., 2024). These temperature differences indicate the presence of strong
175 temperature gradients within the rock mass. In the same way, the Active Layer Thickness (ALT,
176 *i.e.*, the maximum seasonal thaw layer) is also highly variable as interpolated between
177 temperature sensors: it is observed to be around 1.3 to 2.7 m in summer on the NW side, while
178 it reaches 4.8 to 7.6 m on the S side in the early fall. Below this depth, permafrost is present
179 (Magnin et al., 2024). Figure A1 (appendix A) shows the temperature variation over depth in
180 boreholes BH-NW and BH-S on different dates

181 BH-NW is located along an electrical resistivity profile (NW profile) and is positioned
182 between electrodes 8 and 9 (counted from the bottom) of the NW profile (see Fig. 1c). The
183 temperature measured in this borehole is used to assess the accuracy of the temperature derived
184 from ERT results using the petrophysical model presented in the next section.

185

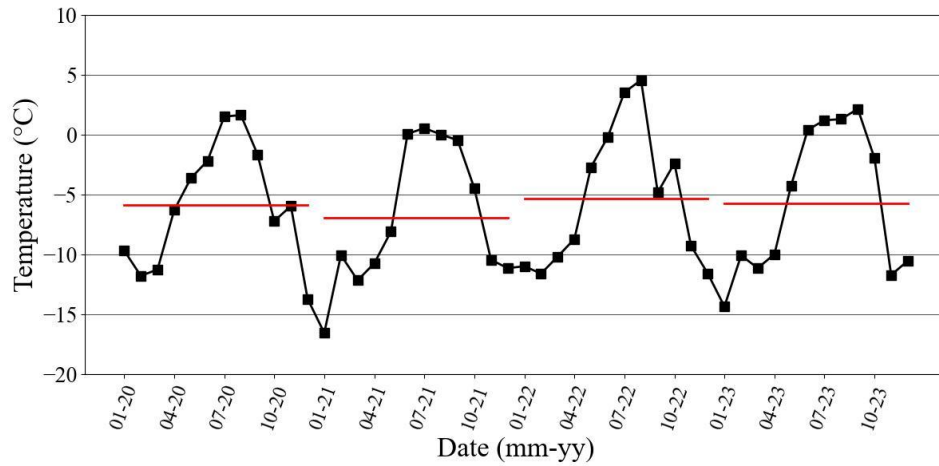
186



187

188 **Figure 1.** Study site location and geophysical survey setting. The yellow lines indicate the approximate
 189 positions of electrical resistivity profiles on each side (NW, E and S profiles). The red dots denote the
 190 borehole locations. (a) Location of the study site (Aiguille du Midi (AdM)), in the Mont Blanc massif
 191 (here, the French side). The electrical resistivity profile and borehole locations at the East face(b), at the
 192 North-West face (c) and at the South face (d).

193



194

195 **Figure 2.** Monthly average air temperature (°C) at AdM during the survey period (Data from the
 196 meteorological station of Institute of Environmental Geosciences at the Aiguille du Midi). Horizontal
 197 bars show the annual average air temperature.

198

199 3. Electrical conductivity - temperature relationship

200 The electrical conductivity of a rock represents its ability to conduct an electrical current
 201 under the application of an imposed electrical field. The electrical conductivity (inverse of the
 202 electrical resistivity) of a rock depends on its porosity ϕ (dimensionless), water content θ
 203 (dimensionless), pore water conductivity, Cation Exchange Capacity (CEC), and rock
 204 temperature T (in °C) (*e.g.*, Revil et al., 1998).

205 Above the freezing point (typically, but not necessary, around 0°C), electrical
 206 conductivity ($\sigma(T)$ in S m^{-1}) increases linearly with temperature according to Revil et al. (1998):

$$207 \quad \sigma(T) = \sigma(T_0)[1 + \alpha_T(T - T_0)], \quad (1)$$

208 where $\alpha_T = 0.021 \pm 0.02 \text{ } ^\circ\text{C}^{-1}$, $T_0 = 25^\circ\text{C}$ denotes the reference temperature, and $\sigma(T_0)$ denotes
 209 the conductivity of the rock at the reference temperature. Equation (1) results from the effect of
 210 temperature on the mobility of the ions in the pore water and in the electrical double layer
 211 coating the surface of the grains.

212 In contrast, under freezing conditions, temperature variations have a significant
 213 influence on electrical conductivity because of the occurrence of an insulating phase (*i.e.*, ice
 214 formation) in the pore space and despite the increase in the salinity of the pore water with
 215 temperature decrease. This temperature dependence of electrical conductivity can be modeled
 216 as follows (see details in Duvillard et al., 2018; 2021; Coperey et al., 2019):

$$217 \quad \sigma(T) \approx \left[(\phi - \theta_r) \exp\left(-\frac{T - T_F}{T_C}\right) + \theta_r \right] \frac{\sigma(T_0)}{\phi} [1 + \alpha_T (T - T_0)], \quad (2)$$

218 where θ_r (dimensionless) denotes the residual water content when $T \ll T_F$, T_F denotes the
 219 liquidus or freezing point/temperature, T_C denotes a characteristic temperature controlling the
 220 transition between the unfrozen state and the frozen state, and $\phi - \theta_r$ denotes the maximum
 221 volumetric ice content at low temperatures. Equation (2) provides the opportunity to convert
 222 electrical conductivity or electrical resistivity tomogram measured in the field to a temperature
 223 distribution (*e.g.*, Duvillard et al., 2021).

224

225 4. Methods

226 4.1 Laboratory measurements

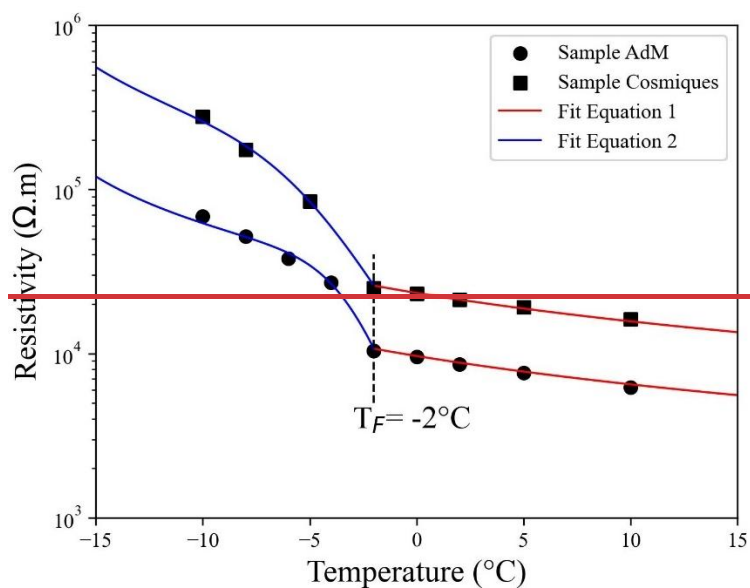
227 In order to calibrate our field measurements and evaluate the parameters (*e.g.*, T_C , θ_r)
 228 in the petrophysical model discussed above (Section 3), we conducted an electrical conductivity
 229 experiment on a granite rock sample collected from an outcrop at the study site. The cube-
 230 shaped granite sample (dimensions: $5 \times 5 \times 5 \text{ cm}^3$) was dried during 24 h at approximately 100
 231 °C, then saturated under vacuum with degassed water. The saturated water conductivity was
 232 0.016 S m^{-1} at equilibrium at $T = 25^\circ\text{C}$. This value is representative of the conductivity of
 233 infiltrating water collected and measured in galleries at the AdM site (approximately $150 \mu\text{S/cm}$
 234 or 0.015 S m^{-1} , see Ben-Asher et al. (2026). The sample was left in the solution for several

235 weeks to reach chemical equilibrium before performing the laboratory measurements. The
236 sample was characterized by a very low measured porosity $\phi = 0.014$.

237 For thermal-resistivity analysis, the sample was placed in a heat-resistant insulating bag
238 immersed in a thermostat bath (KISS K6 from Huber; dimensions: 210×400×546 mm³; bath
239 volume: 4.5 L). The temperature of the bath was controlled with a precision of 0.1 °C. Glycol
240 was used as the heat carrying fluid (Coperey et al., 2019). Thin Carbon film electrodes were
241 used for both current injections and potential measurement. The complex conductivity spectra
242 were obtained over the temperature range of +10 to -10 °C, using a high-precision impedance-
243 meter ZEL-SIP04-V02 (Zimmermann et al., 2008). The resistivity measurements reported here
244 are at a frequency of 1 Hz (Coperey et al., 2019).

245 ~~Figure 3 presents the measurement results for the granite sample from the study site~~
246 ~~(labeled Sample AdM), alongside measurements of another granite sample (Sample~~
247 ~~Cosmiques) collected from a nearby site at the lower Cosmiques Ridge (Mont Blanc massif,~~
248 ~~3613 m a.s.l.), as reported by Duvillard et al. (2021). The experimental datasets are presented~~
249 ~~along with data fits, using Equations 1 for temperatures above the freezing point, and Equation~~
250 ~~2 for temperatures below the freezing point. The model proposed in Section 3 successfully fits~~
251 ~~the data above and below the freezing temperature, providing a proxy for connecting electrical~~
252 ~~conductivity to temperature.~~

253



254
 255 **Figure 3.** Resistivity temperature relationship from laboratory measurements on two granite samples
 256 from (1) the study site (Sample AdM), and (2) from the Cosmiques ridge, Mont Blanc massif, West
 257 (3613 m a.s.l.) (Sample labeled Cosmiques). T_F denotes the freezing temperature. The solid lines
 258 correspond to the fits using the Equation 1 (red lines) and Equation 2 (blue lines), in unfrozen and frozen
 259 conditions, respectively. The parameters of the model in Equation 2 are ($T_C = 1.3^\circ\text{C}$, $\theta_F = 0.004$, $\sigma(T_0) =$
 260 $2.3 \times 10^{-4} \text{ S m}^{-1}$) for Sample AdM, and ($T_C = 2.17^\circ\text{C}$, $\theta_F = 0.004$, $\sigma(T_0) = 9.5 \times 10^{-5} \text{ S m}^{-1}$) for Sample
 261 Cosmiques.
 262

263 4.2 ERT Data acquisition

264 ERT has been conducted over a four-years period (06/2020 - 12/2023). A total of three
 265 cables, each with 32 take-outs spaced 5 m (for a profile length of 155 m), were installed. The
 266 three cables were deployed downwards from the summit in three directions: North-West (NW),
 267 East (E) and South (S). The S profile starts at the South side and passes to the North-West side
 268 around mid-distance (see Fig. 1c, d). The cables ~~were installed~~ ~~ation was~~ gradually (over a year)
 269 starting from NW side (installed in June 2020), then on the South side (installed in July and
 270 August 2020), and finally on the East side (installation finished in March 2021 because of
 271 snowpack in 2020 at this side). In order to ensure good electrical contact between electrodes
 272 and rock mass, stainless steel (A4/316) climbing bolts (Fischer 10×126 mm) poured in salty
 273 bentonite were used and placed firmly in holes drilled in the rock. A specially designed jumper

274 was used to attach each take-out to the bolt to ensure maximum contact. The resistivity cables
275 were attached to anchors to minimize damage from rockfall and snow pressure.

276 A LS2-Terrameter (ABEM) with internal impedance of 20 M Ω was used for the data
277 acquisition. The ERT device and control system for monitoring were deployed inside the
278 summit station with network access, power connection, and overvoltage protection. Data
279 acquisition was fully automated and remotely controlled since September 2021. Finally, the
280 position of every electrode was measured using a differential GPS when the signal is available
281 and a theodolite in steep areas. The measurements were carried out using a Wenner
282 configuration, which provides a high signal-to-noise ratio and is widely used in mountain
283 permafrost environments (Mollaret et al., 2020; Krautblatter and Hauck, 2007; Dahlin and
284 Zhou, 2004). Each profile consists of 155 data points. An injected current ranging from 0.1 mA
285 to 200 mA was applied, with a maximum stack number of 4 was applied to ensure a standard
286 deviation of less than 5 % in the measured resistivity. The first measurements were performed
287 in June 2020. Between June 2020 and September 2021, ERT measurements were repeated
288 occasionally. Then the continuous measurements started in late September 2021 after
289 developing an automated system of acquisition. Datasets were daily recorded for each profile
290 (NW, S and E profiles).

291 A Contact Resistance (CR) test was performed before each series of measurements. A
292 high contact resistance in the rock wall (>100 k Ω) was encountered throughout the entire survey
293 period, which posed a challenge to the quality and continuity of data acquisition. CR varies
294 between a few k Ω and 10 000 k Ω . However, beyond a CR threshold, the ERT measurements
295 lose their accuracy. Electrodes with high CR (>600 k Ω) are excluded automatically by the LS2,
296 leading to gaps in the pseudo-section of apparent resistivity. Special efforts were made to reduce
297 CR and improve the electrode/rock contact, including the addition of salty water, using copper
298 electrodes and duplicate electrodes. The latter one resulted in a significant and durable

299 improvement in CR (one order of magnitude reduction in CR). Figure B1 shows the temporal
300 evolution of CR at profiles S and NW, as well as gaps in the A-ERT measurements caused by
301 cable defects. ~~It also The indicates the date of duplicate electrode installation, highlighting a~~
302 ~~reduction in contact resistance following installation periods highlighted by dotted lines~~
303 ~~correspond to time intervals during which comparison of CR before and after electrode~~
304 ~~doubling can be made.~~

305 The A-ERT ran into numerous software and hardware issues, resulting in unsystematic
306 data gaps. The E face cable was severely damaged by a lightning strike, before being destroyed
307 by an uncontrolled rock purge. Additionally, NW and S cables were both damaged by rockfalls,
308 leading to significant data gaps (see Fig. 34 and Fig. B1). Repairing or replacing the damaged
309 cables was not possible for several reasons (e.g., limited access to the cable path because of
310 accumulated snowpack). Data acquisition on the Eastern side (E profile) encountered numerous
311 challenges related to contact resistance, rockfalls and cable connections, resulting in long gaps
312 and insufficient data for long time analysis or time-lapse inversion.

313

314 4.3. Data processing and inversion

315 The apparent resistivities were calculated using the open-source package pyGIMLi
316 (Rücker et al., 2017), which combines measured resistances and electrode positions. ~~Figure 4~~
317 ~~shows the temporal distribution of the measured apparent resistivities and the averaged apparent~~
318 ~~resistivity along the S profile, with examples of time series of measured apparent resistivities~~
319 ~~obtained using various quadrupole configurations (ABMN), shown in different colors. The~~
320 ~~majority of measured apparent resistivities are distributed over three orders of magnitude (100~~
321 ~~$\Omega\cdot\text{m}$ to 100 k $\Omega\cdot\text{m}$), with few data points out of this range.~~

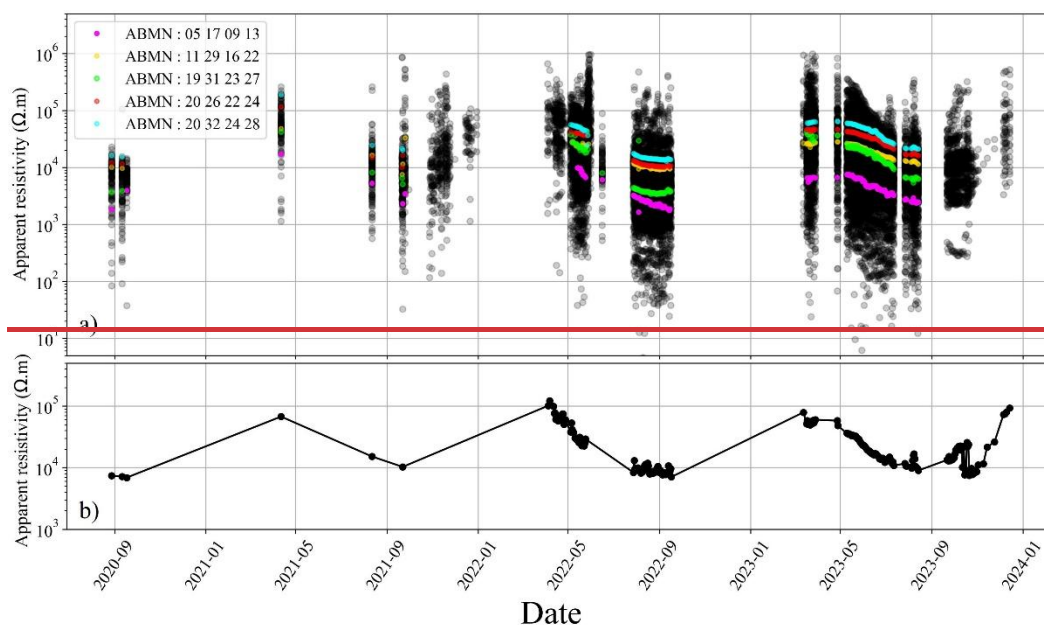


Figure 4. Distribution of measured apparent resistivity. a) daily distribution of the apparent resistivity over time at the S face (approximately 300 datasets). Colored lines present examples of resistivity times series, each corresponding to a different set of quadrupoles (AMNB). b) Mean daily measured apparent resistivity at the S face.

For datasets used in inversion, a systematic quality-control procedure was applied prior to processing. The primary selection criterion was the number of connected electrodes within each pseudo-section. Up to four unconnected electrodes (typically due to high contact resistance) were tolerated, depending on their positions, since electrode contributions are not equal in the pseudo-section. After selecting valid datasets, outlier removal was performed. To define appropriate filtering threshold, we individually analyzed representative pseudo-sections acquired in autumn and spring (completed datasets). As a result of this analysis, we filtered outliers out of the range (300 Ωm - 20 $\text{k}\Omega\text{m}$) for data measured in summer and autumn, and out of range (300 Ωm - 200 $\text{k}\Omega\text{m}$) for data measured in spring and winter. Table C1 (appendix C) summarizes the data presented in this study. In most cases, more than 80 % of the originally recorded data points were retained in each pseudo-section after filtering.

The inversion of the electrical resistivity datasets was performed using the open-source package pyGIMLi (Rücker et al., 2017; Günther et al., 2006). The inversion uses a Gauss-

341 Newton minimization algorithm of a cost-function penalizing the roughness of the electrical
342 resistivity distribution on an irregular grid (Günther et al., 2006). In the absence of a reciprocal
343 dataset to estimate errors in measurements, we used a linear error model which assumed 5 %
344 relative error and absolute error $1e-5$. The parameters used in the inversion process are $zWeight$
345 = 10 and smoothness (λ) equal one. The inversion parameter $zWeight$ is chosen higher
346 than one to enhance the vertical discontinuities and vertical structures (*i.e.*, to better delineate
347 the active layer, and infrastructures), during the inversion process. Following Mollaret et al.
348 (2020), Then, an iterative process was conducted to select the smoothness parameter (λ)
349 that minimizes the data misfit of individual inversions of a reference dataset (dataset of
350 30/06/2020). The root-mean-square (RMS) error is evaluated at the end of each inversion and
351 reported at the figures. In order to track the seasonal and interannual variations in the
352 permafrost, a time-lapse inversion approach was employed. In this case, the reference model
353 was moved along with the inversion so that the difference to the preceding step is constrained
354 (Doetsch et al., 2015; Karaoulis et al., 2013).

355

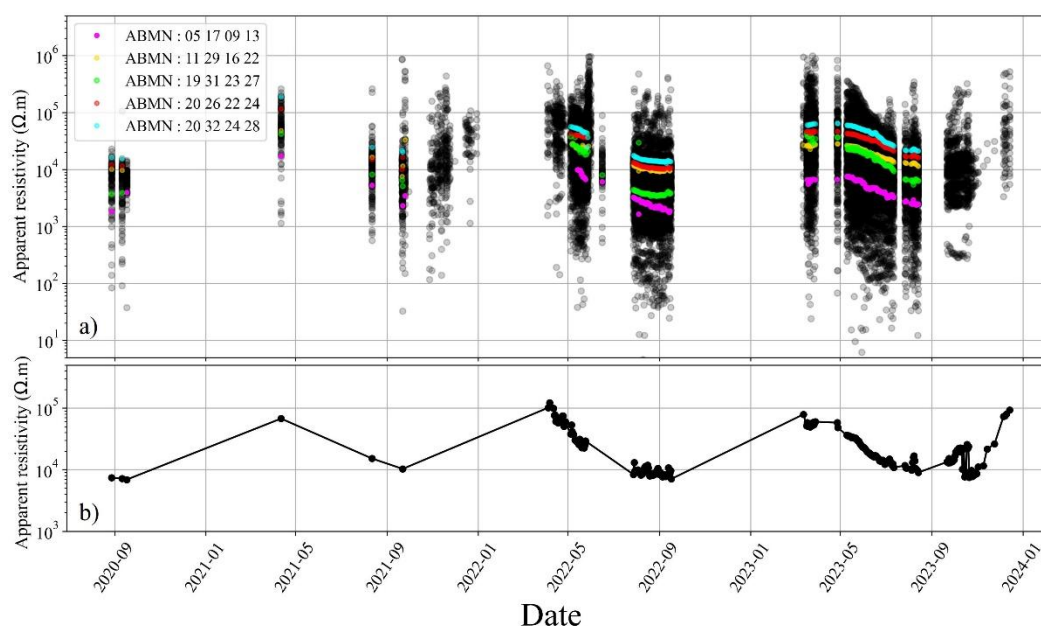
356 5. Results and interpretation

357 Selected datasets are presented below to address the objectives of this study, including
358 the characterization of the general structure, seasonal variations, and the hydrogeological
359 system.

360 5.1. Overview of the raw data

361 Our interpretation of the ERT data starts with an analysis of the measured apparent
362 resistivity data, which can provide insights into subsurface conditions. Figure 3 shows the
363 temporal distribution of the measured apparent resistivities and the averaged apparent resistivity
364 along the S-profile, with examples of time series of measured apparent resistivities obtained
365 using various quadrupole configurations (ABMN), shown in different colors. The majority of

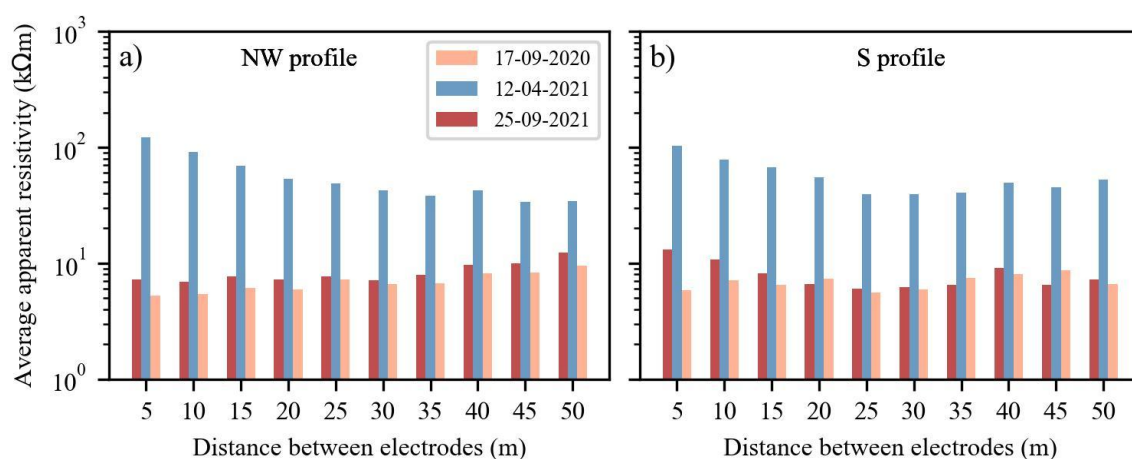
366 measured apparent resistivities are distributed over three orders of magnitude (100 Ω .m to 100
 367 k Ω .m), with few data points out of this range.



368
 369 Figure 3. Distribution of measured apparent resistivity. a) daily distribution of the apparent
 370 resistivity over time at the S face (approximately 300 datasets). Colored lines present examples of
 371 resistivity times series, each corresponding to a different set of quadrupoles (AMNB). b) Mean daily
 372 measured apparent resistivity at the S face.

373 Figure 45 shows the variations in the average apparent resistivity associated with the
 374 same electrode distance or pseudo-depth for three selected datasets from two profiles (NW and
 375 S profiles). The data reveal the interannual and seasonal variations in the measured apparent
 376 resistivity, as well as the differences between the two sides. During frozen conditions at the
 377 surface (dataset from 12-04-2021), the apparent resistivity is almost the same on both sides
 378 (~ 100 to 120 k Ω m near the surface), with only a slight decrease with depth at both sides. At the
 379 end of summer (dataset from 17-09-2021 and 25-09-2021), the resistivity values are higher in
 380 2021 than in 2020 on both sides, which correlates with climatic data indicating that 2021 was a
 381 cooler year, on average (see Fig. 2). Secondly, on the NW face, the average resistivities increase
 382 with depth (from ~ 7 k Ω .m to ~ 12 k Ω .m), while on the south side, the average resistivities

383 decrease with depth (approximately 13 k Ω .m at shallow depth to \sim 7 k Ω .m at greater depth).
 384 This difference in trend between the two sides can be attributed to cooler conditions on the
 385 north-face, where permafrost appears at shallow depth, and warmer conditions on the south-
 386 face, characterized by a drained and thicker thawed active layer. This observation is consistent
 387 with the temperature measurements from boreholes BH-NW and BH-S (see Fig. A1).
 388



389
 390 **Figure 45.** Seasonal variations of the average apparent resistivity at different distances between
 391 electrodes within a quadrupole (*i.e.*, at varying depths of investigation). Data in spring shows the same
 392 pattern on both sides. In autumn, there is a divergence in the trend of average resistivities with depth on
 393 both sides, that is related to the hydrothermal conditions at each side.

394

395 5.2. Internal structure of the site

396 In order to gain an overview of the internal structure of the study site based on the
 397 resistivity distribution, we carried out inversions of the first dataset acquired along two long
 398 profiles (NW+S and NW+E), usingaequired-with Wenner electrode arrays with 64 electrodes
 399 (Figs. 5 and 6). Figure 65 shows the electrical resistivity tomogram from late summer 2020
 400 (August 26th, 2020), where acquisition on both North-West and South sides (NW+S) was
 401 performed. The tomogram clearly reveals the site's internal structure, with low resistivity areas
 402 (warm-colored zones) indicating the relative positions of the infrastructure elements (elevator
 403 and galleries on both sides). It also shows the extent of the active layer (moderate resistivity

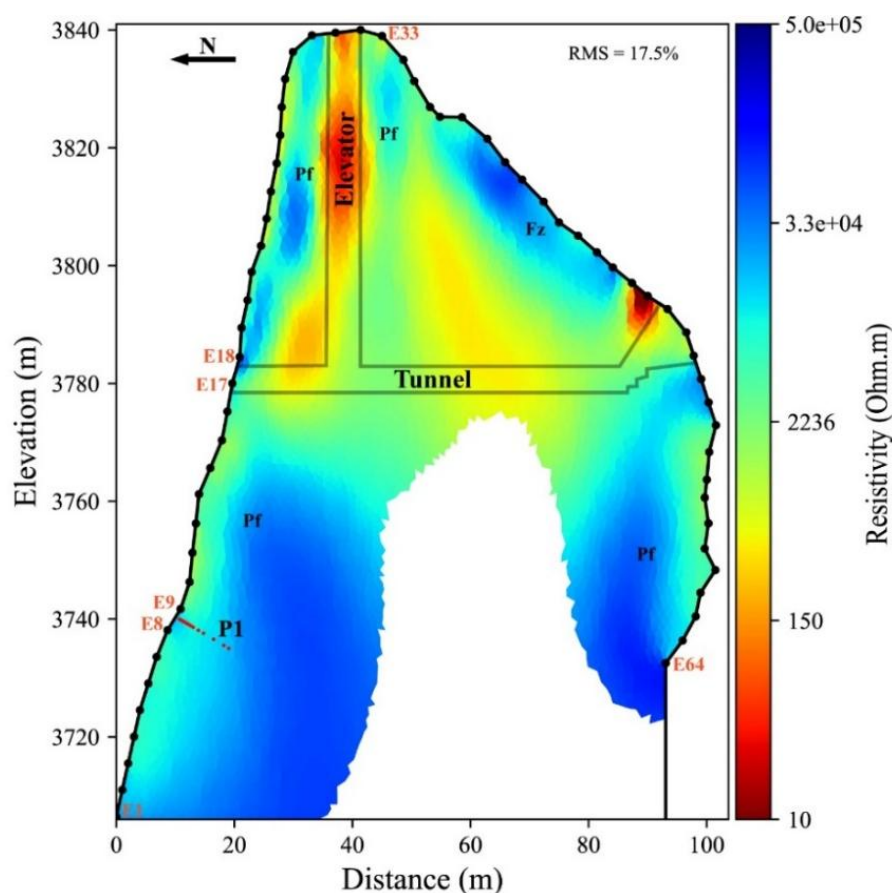
404 areas near the surface), as well as the permafrost evidenced by high resistivity areas
405 (represented in cool colors). Although the lower part of the tomogram appears similar on both
406 the NW and S profiles, which is expected since they lie in rockwalls that are alike regarding
407 slope and aspect (where the lowest part of the S profile is deployed on the NW face as well, see
408 Fig 1c), significant differences are evident in the upper part (*i.e.*, above the gallery level), these
409 differences highlight revealing the contrast between the sun-exposed S face, composed (S-side
410 of fractured granite (clearly visible in the field; see Fig. 1d) and exposed to strong insolation,
411 leading to drier surface conditions and consequently higher electrical resistivity. In contrast, the
412 and-shaded NW face (NW-side mainly consisting of massive granite and less influenced by
413 mostly dependent on the sensible atmospheric heat flux), remains wetter and thus leads to lower
414 resistivity close to surface. The upper part of the profile therefore reveals strong thermal
415 gradient typical of high-alpine summits (Noetzli et al., 2007; Magnin et al., 2017). The high-
416 resistivity area thus appears limited, likely due to the heat flux from the sun-exposed and warm
417 face towards the close shaded-face.

418

419

420

421



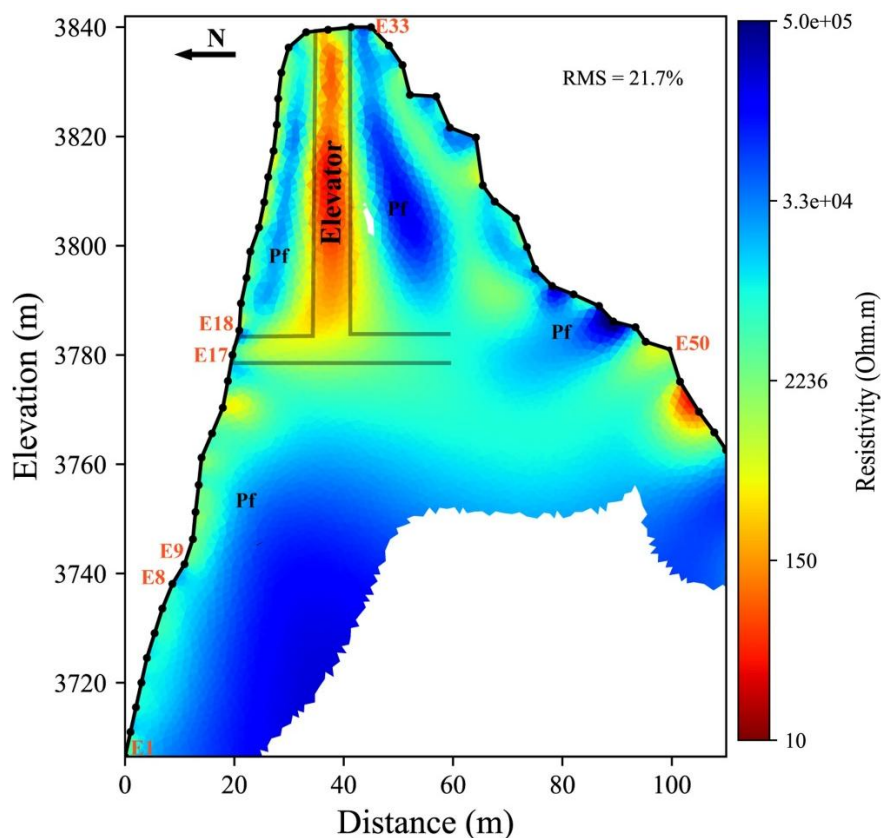
422

423 **Figure 56.** Electrical resistivity tomogram over the NW+S profile measured on August 26, 2020. A total
 424 of 320 data points used for the inversion (475 data points constitute the complete pseudo-section), about
 425 30% of dataset was filtered). Grey lines indicate the approximative positions of infrastructure (galleries
 426 and elevator). Pf stands for Permafrost zone and Fz for Fractured zone. E1 to E64 are Electrode
 427 numbers. Red dots at P1 indicate positions of the thermal sensors in BH-NW.

428

429 Figure 67 provides an example of the resistivity tomogram for the combined NW and E profiles.

430 This tomogram highlights the changes in resistivity associated with permafrost, active layer,
 431 and anthropogenic installation (such as the elevator and gallery (relatively far from the profile
 432 at the E side compared to S profile)). On the eastern side, a thick and desiccated active layer (>
 433 5 m depth) is observed, with some resistive zones near the surface. Indeed, these resistive zones
 434 are likely fractured zones creating an unsaturated and air-filled zone and surrounded by
 435 moderate resistivity regions where fractures are filled or where water drainage is weak or
 436 absent.



437

438 **Figure 67.** Electrical resistivity tomogram over the profile NW+E at the end of summer (September 25
 439 th, 2021). A total of 310 data points were used for the inversion (475 data points constitute the complete
 440 pseudo-section), about 35% of dataset was filtered). ~~Data acquisition on the East profile run into~~
 441 ~~problems related to electrodes contact and cable malfunction.~~The last 10 electrodes from the E profile
 442 were removed during processing due to connection issues. Pf stands for Permafrost zone

443

444

445 5.3. Seasonal and interannual variations

446

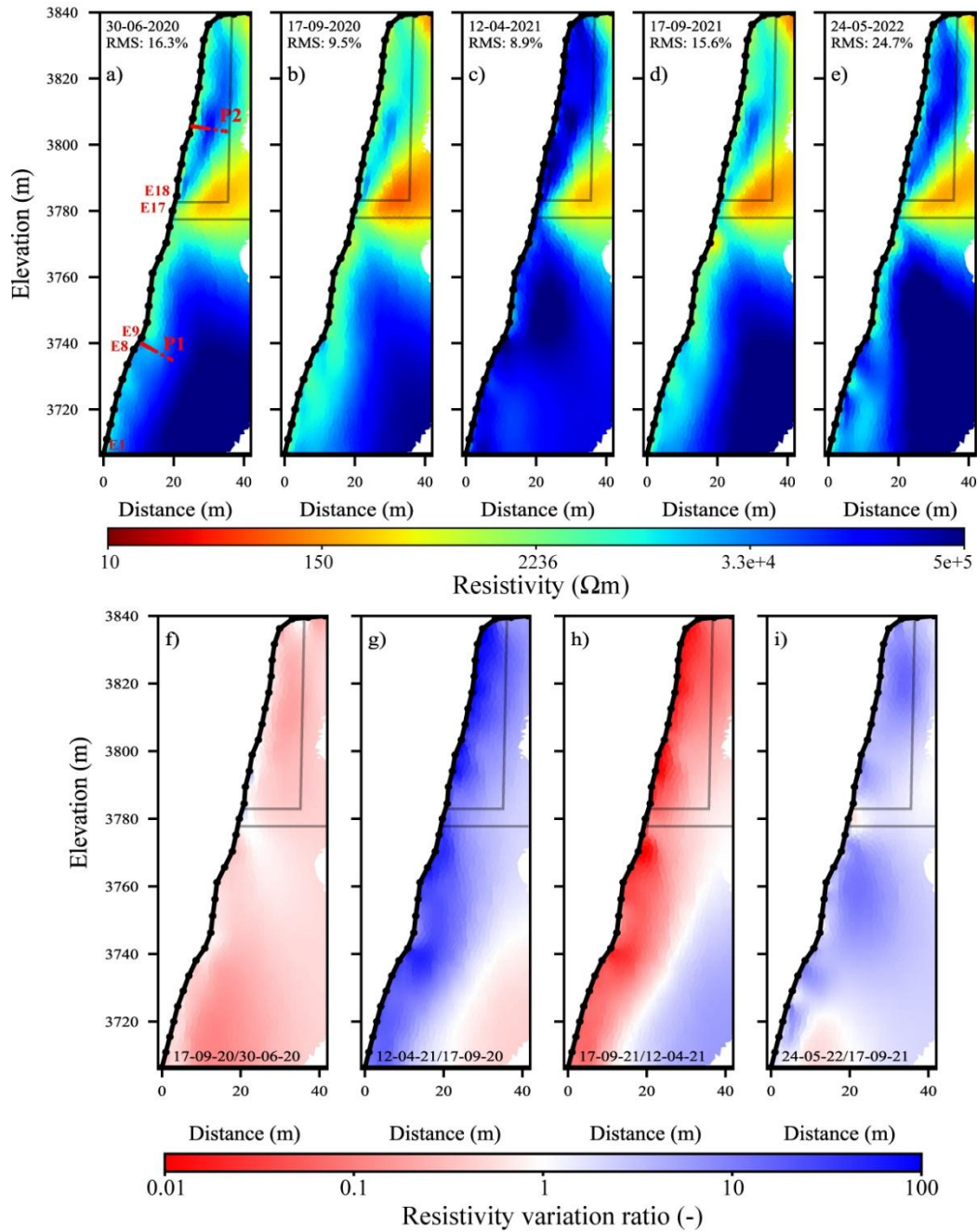
447 In order to track the seasonal and interannual variations in the permafrost, a time-lapse
 448 inversion approach was employed to invert datasets for each profile (NW, S), while the data at
 449 the east profile was excluded from this analysis due to significant data gaps caused by poor
 450 electrical connection and cable malfunctions. Figure 8-7 shows the tomograms of resistivity
 451 distribution after a time-lapse inversion of selected datasets acquired along the NW profile at
 452 different time intervals. A more complete times series is presented in appendix D, while the
results from the south profile are discussed in section 5.6). Spatial and temporal changes in

453 resistivity can be observed, while the anomaly related to the gallery (the warm-colored area
454 (low resistivity area) remains relatively consistent over time. The permafrost layer associated
455 with high resistivity, is observed in two zones, above and below the gallery. 2021 was, on
456 average, cooler than both 2020 and 2022 in coherence with air temperature (Fig. 2), and this is
457 reflected in the tomograms by a more prominent cool-colored zone (indicating colder
458 conditions) in 2021 compared to data in 2020 (Fig. 78b and d). Additionally, there is a
459 significant variation in the lower part of the tomograms in 2022 (Fig. 78e), which may be related
460 to water infiltration in fractures that shortcut the heat transfer from the surface to depth (Hasler
461 et al., 2011). However, this area is uncertain, as it is located at the border of the tomogram
462 where sensitivity is low. In addition, the RMS error is high in this tomogram, indicating high
463 uncertainties. Therefore, this information should be carefully considered and verified with
464 further measurements focused on the zone of interest. Unlike Offer et al. (2025), no evidence
465 of water pressurization was observed from the geophysical measurements on the NW face. This
466 is most likely due to the distance between the monitored area and the water table laying at about
467 1000 m lower (Magnin and Josnin, 2021), and that leads to water drainage.

468 Instead of analyzing temporal resistivity changes in absolute terms, Figure 78 (f - i)
469 illustrates the resistivity variation ratio between two subsequent measurements. This approach
470 facilitates the tracking and visualization of small changes in resistivity. A value of 1
471 (represented in white color) corresponds to no change in resistivity between the two
472 measurements (reflecting consistent thermal/hydrological geological conditions, topographic
473 effects, infrastructure or no considerable change in temperature over time), while the blue color
474 indicates that the resistivity increased over time, and the red color represents the inverse. It can
475 be observed that seasonal variations are the most pronounced, as illustrated in Figure 78g, h
476 and i, compared to short-term fluctuations (see Fig. D2). The effects of freezing and thawing
477 are marked by maximum variations near the surface (in the active layer). In contrast, over a

478 short time interval (*i.e.*, a few weeks), only minor variations are noted (*e.g.*, Fig. 78f, Fig. D2
479 b, e and j). The decrease in resistivity near the surface at approximately 3780 m, observed in
480 Figure 78i, could be related to water flow around the gallery, where water circulation and
481 percolation in the galleries occurs every summer (Ben-Asher et al., 2025). Consequently, a
482 specific water diversion system has been installed to protect tourists from these water flows.
483 Furthermore, at approximately 3740 m, close to borehole BH-NW, we observe variations in
484 resistivity, with values higher than in the surrounding zone, forming a vertical pattern visible in
485 Figures 78b, d, and e. These features coincide with open sub-vertical fractures that affect the
486 temperature-depth profile in boreholes (Magnin et al., 2015). ~~Extended times lapse inversion
487 of datasets from NW and S face are presented in appendix D.~~

488



489

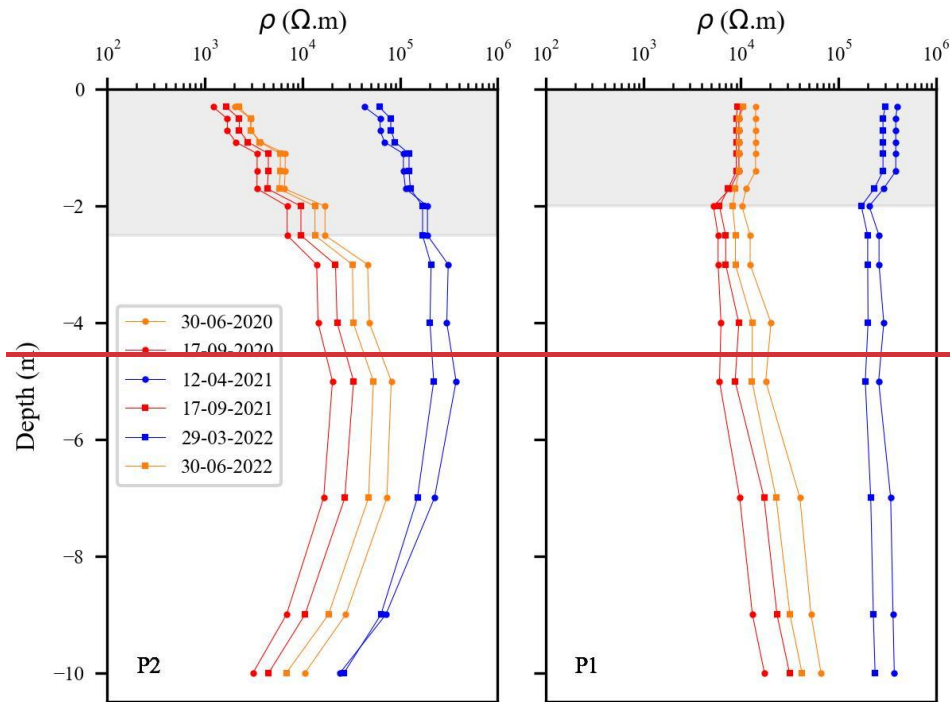
490 **Figure 78.** Seasonal and interannual variations of electrical resistivity at NW side. a - e) electrical
 491 resistivity tomograms at different dates (from June-2020 to June-2022). The conductive zone (in warm
 492 colors) denotes the presence of the gallery and elevator (see Fig. 56). The red dots (P1 in panel a) indicate
 493 the positions of the thermal sensors in the borehole BH-NW. Data presented on Figures 89, 10 and 11
 494 are extracted at the red dots (P1 and P2). f - i) resistivity variation ratio between consecutive electrical
 495 resistivity tomograms. Blue colors indicate an increase in resistivity, while red colors represent a
 496 decrease in resistivity from one measurement to the next.

497

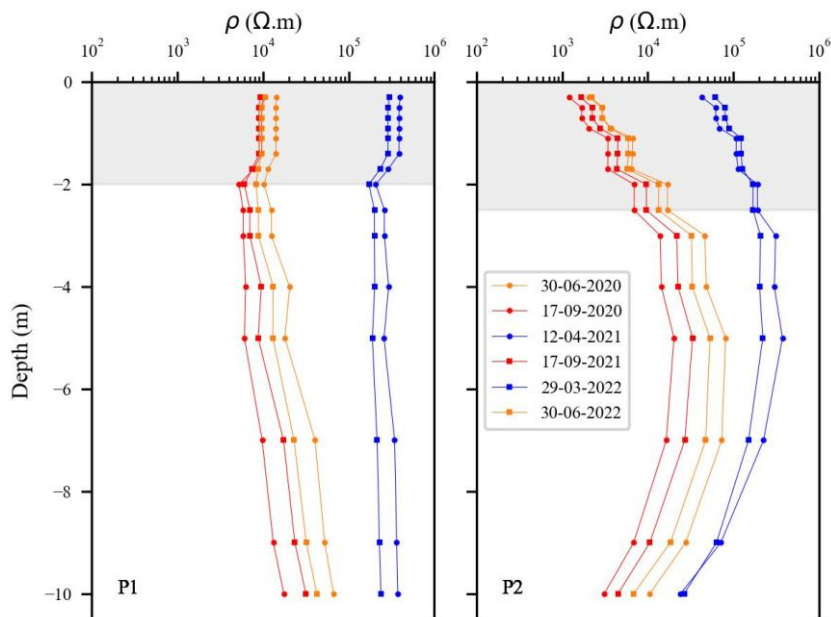
498

5.4. Virtual borehole analysis

Inverted resistivities were extracted along profiles P1 and P2, corresponding to borehole BH-NW and a virtual borehole, respectively (see positions of P1 and P2 in Fig. 78a). The extracted resistivities (Fig. 89) show that the variation of resistivity with depth is more pronounced at P2 than at P1. This greater variation could be due to a higher water content in the active layer or a thicker active layer at P2 compared to P1. The greater thickness of the active layer in the upper section can be explained by the 3D heat transfer and the proximity of the shaded face (NW side) to the sun-exposed faces (S side) in the top part (Magnin et al., 2017), as well as the greater amount of direct sun-beams at the summit than in the more shaded lower parts of the face. The 3D effects are well visible at depth of P2, where resistivity decreases due to warmer conditions close to the opposite sun-exposed face. In the lower section at P1, the contrast between the resistivity in the active layer and that in the permafrost is not significant. This may be attributed to (i) reduced thermal variability because of snow accumulation in this zone (see Fig. 1c), where the snowpack acts as a thermal insulator, reducing temperature variability ~~and leading to lower water content in the active layer~~; (ii) the presence of fractures (as noted above) influencing the temperature-depth profile (see Fig. 87b, e and d). However, it is important to note that the ALT is about 2.7 m at the end of summer (based on BH-NW measurements; see Fig. A1), whereas, the smallest quadrupole spacing is 15 m, leading to effective depth around 2.55 m (Edwards, 1977), which is insufficient to fully capture ~~the whole~~ the resistivity variations ~~close near the~~ ~~to~~ surface. Additionally, a slight decrease in permafrost resistivity is observed between 30 June 2020 and 30 June 2022. That is consistent ~~coherent~~ with the observed permafrost warming at 10 m depth (Magnin et al., 2024). Finally, in 2021, resistivity values were higher in both the upper and lower parts (at P1 and P2) compared with 2020 and 2022, consistent with the temperature measurements (see Fig. 2, or details in Magnin et al. (2024)).



524



525

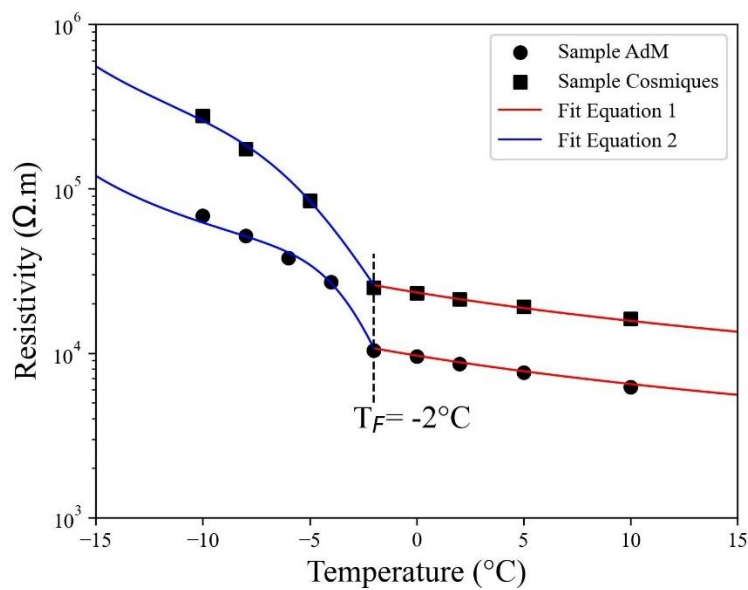
526 **Figure 98.** Resistivity extracted over depths at different dates and locations (P1, P2). Resistivities are
 527 extracted from tomograms in Fig. D1. There is greater variation at the higher profile (P2), where heat
 528 transfer from the nearby sun-exposed faces is more significant in the site's upper part.

529

530 **5.54. Temperature - resistivity relationship**

531 Figure 9 presents the measurement results for the granite sample from the study site
 532 (labeled Sample AdM), alongside measurements of another granite sample (Sample

533 Cosmiques) collected from a nearby site at the lower Cosmiques Ridge (Mont-Blanc massif,
 534 3613 m a.s.l.), as reported by Duvillard et al. (2021). The experimental datasets are presented
 535 along with data fits, using Equations 1 for temperatures above the freezing point, and Equation
 536 2 for temperatures below the freezing point. The model proposed in Section 3 successfully fits
 537 the data above and below the freezing temperature, providing a proxy for connecting electrical
 538 conductivity or electrical resistivity measured in field to temperature.



540

541 **Figure 9.** Resistivity-temperature relationship from laboratory measurements on two granite samples
 542 from (1) the study site (Sample AdM), and (2) from the Cosmiques ridge, Mont-Blanc massif, West
 543 (3613 m a.s.l.) (Sample labeled Cosmiques). T_F denotes the freezing temperature. The solid lines
 544 correspond to the fits using the Equation 1 (red lines) and Equation 2 (blue lines), in unfrozen and frozen
 545 conditions, respectively. The parameters of the model in Equation 2 are ($T_C = -1.3$ °C, $\theta_r = 0.004$, $\sigma(T_0) =$
 546 2.3×10^{-4} S m⁻¹) for Sample AdM, and ($T_C = -2.17$ °C, $\theta_r = 0.004$, $\sigma(T_0) = 9.5 \times 10^{-5}$ S m⁻¹) for Sample
 547 Cosmiques.

548

549 Extracted resistivities at P1 are superimposed on the co-located borehole BH-NW,
 550 where temperature measurements are available. We are using these two datasets (*i.e.*,
 551 temperature and resistivity measurements at the same location, BH-NW) to explore the
 552 potential for estimating temperature based on electrical resistivity measurements and to perform

553 a quantitative evaluation of the ~~t~~Temperature - ~~r~~Resistivity relationship determined in a
554 laboratory.

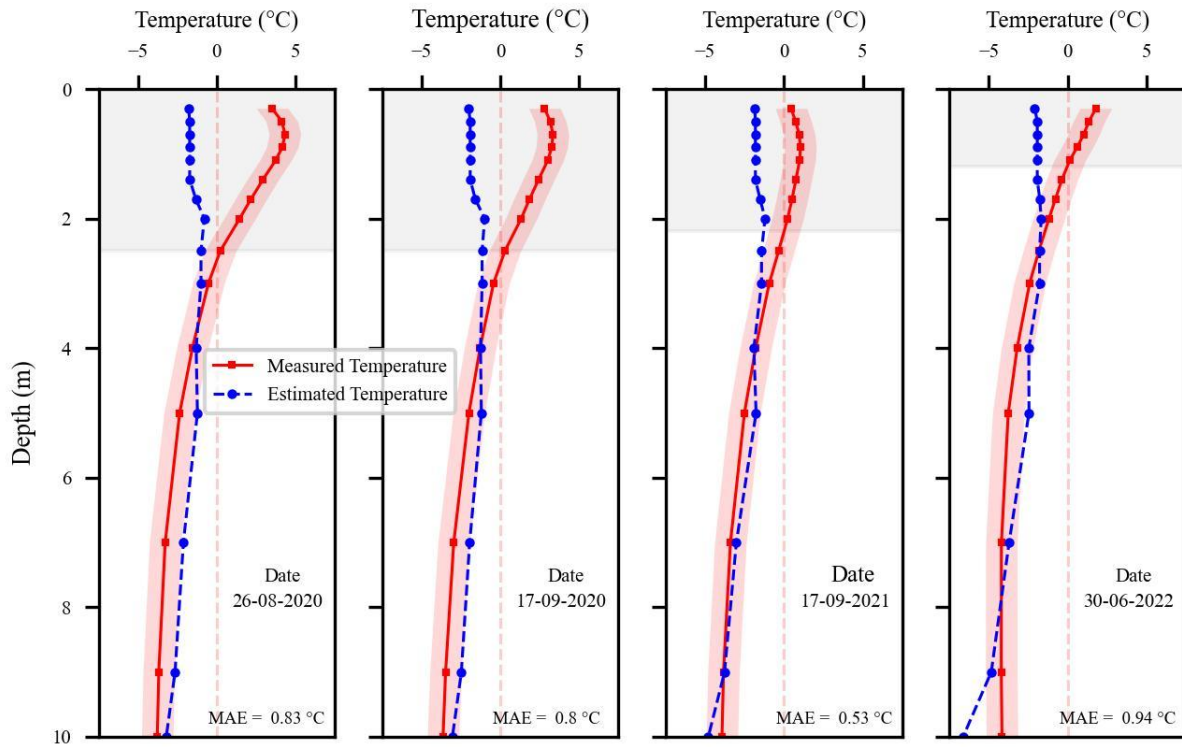
555 It is ~~well established known~~ that, when temperature > 0 °C (*i.e.*, the case in the active
556 layer), ~~electrical~~ resistivity depends on multiple ~~factors, variables~~, including porosity, water
557 content, water salinity, Cation Exchange Capacity (CEC) and temperature (Revil et al., 2018).
558 ~~; This multiple parameter dependance which~~ makes it difficult to ~~accurately~~ model or predict
559 ~~electrical the~~ resistivity, ~~or to use it as a proxy for temperature estimation value~~ in the active
560 layer. In contrast, under frozen conditions, resistivity of ~~a the~~ medium is primarily controlled
561 by the remaining unfrozen pore water ~~content~~, ~~which is largely and is assumed to be temperature~~
562 ~~dependent, on temperature~~, while ~~the~~ other parameters ~~can be assumed relatively remain~~
563 constant.

564 ~~Based on this assumption. Therefore,~~ the ~~resistivity values~~ extracted ~~from resistivities~~
565 ~~inverted model of resistivity in the frozen zone~~ were converted to temperature using the
566 petrophysical model in Equation 2 (Duvillard et al., 2021; 2018; Coperey et al., 2019). Figure
567 10 shows the measured temperature alongside the estimated temperature from ERT data, plotted
568 against depth at different dates (in summer and autumn). A good agreement ~~canis be~~ observed
569 between the measured and estimated temperature in frozen ~~zoneconditions~~, with ~~mean absolute~~
570 ~~error (MAE) differences of~~ less than ± 1 °C ~~within the frozen zone (approximately from 2-2.5~~
571 ~~m to 10 m, depending on the date). at depths between 4 and 10 m. These results suggest that the~~
572 ~~temperature distribution across the site can be reasonably estimated using this model, assuming~~
573 ~~that the medium is sufficiently homogeneous and that resistivity variations are predominantly~~
574 ~~controlled by temperature. This suggests that temperature distribution across the site can be~~
575 ~~calculated using this model (e.g., Duvillard et al., 2021), assuming the medium is homogenous~~
576 ~~and resistivity variations are solely attributed to temperature.~~ Figure 11 illustrates the
577 temperature distribution along the profile NW estimated from electrical resistivity

578 measurements acquired at different dates between June 2020 and June 2022. The estimated
579 temperatures ~~vary consistently~~ with previous the analyses and highlight presented above,
580 ~~revealing~~ two permafrost zones located above and below the gallery. A clear As rock surface
581 ~~temperature was measured in the galleries as well for other purposes, we can also highlight that~~
582 ~~the positive temperature reaching up to 4°C around the gallery is in very good agreement with~~
583 ~~these measurements (Ben Asher et al., 2025). It can be observed a coherent temperature~~
584 ~~gradient with through depth is observed on the 2D temperature sections, with p and positive~~
585 temperatures around and in the infrastructure. It can also be observed that temperature decreases
586 with depth, reaching values lower than -5 °C in the zone where ERT sensitivity is low or absent
587 (see lower part of profile NW Fig 11). At greater depths, the reduced sensitivity affects the
588 reliability of temperature estimates.

589 ~~Finally, urthermore,~~ data collected under frozen surface conditions (*i.e.*, measured in
590 winter and early spring, when with high contact resistance is high) show large discrepancy
591 between the estimated and measured temperature and therefore cannot be reliably used for
592 temperature estimation.

593

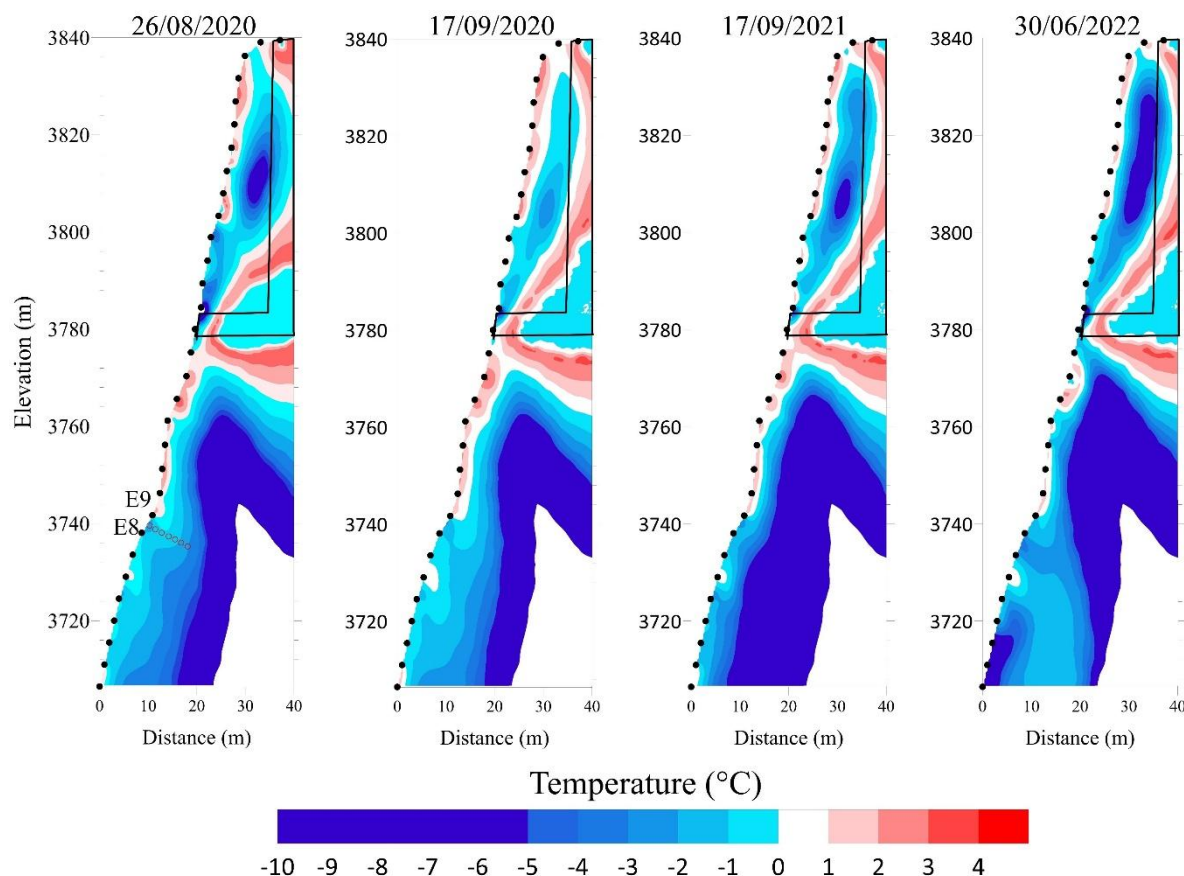


594

595 **Figure 10.** Comparison between measured temperatures in BH-NW and estimated temperatures derived
 596 from geophysical measurements (*i.e.*, extracted resistivity values at different dates) using the
 597 petrophysical model in Equation 2. The gray-shaded area indicates the extent of the active layer at the
 598 time of measurement. The red-shaded zones show the ± 1 °C range around the measured temperature.
 599 The mean absolute error (MAE, in °C) quantifies the average error within the frozen zone for each date.

600

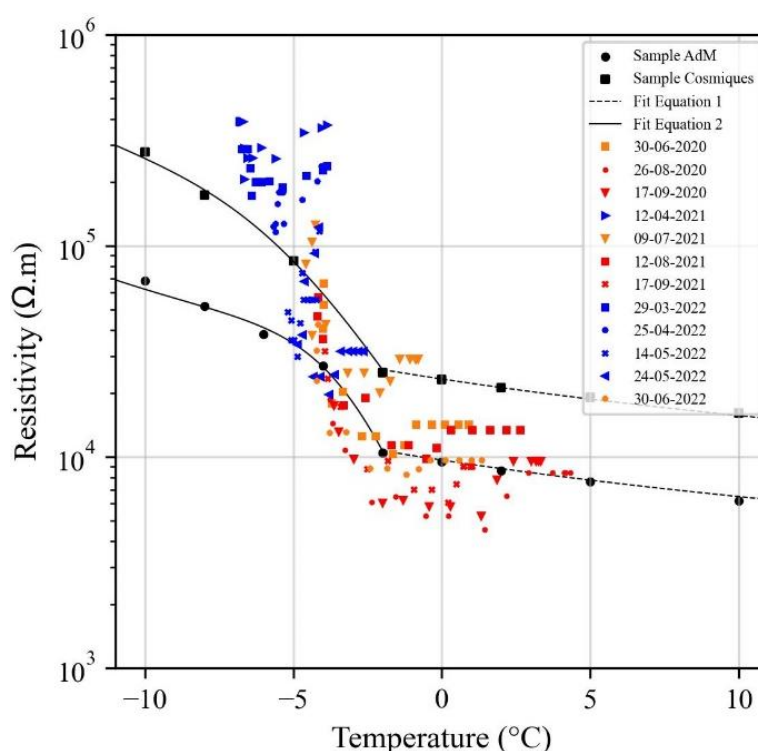
601



602
 603 **Figure 11.** Spatio-temporal evolution of subsurface temperatures along the NW profile derived from
 604 electrical resistivity measurements, using Equation (2) and parameters obtained from laboratory
 605 measurements. Black dots indicate the electrode positions. The red circles indicate the location of
 606 borehole BH-NW, while the black lines mark the relative positions of the gallery and the elevator. The
 607 blanked zones in the lower part of the profile correspond to areas of low sensitivity of the geophysical
 608 measurements and are therefore not reliable to temperature estimation.

609
 610 To go further in our analysis, Figure 12 shows the extracted resistivity at P1 vs.
 611 temperature data measured in co-located BH-NW at different dates. Laboratory measurements
 612 on two granite samples (labeled Sample AdM and Sample Cosmiques) are also shown. Three
 613 key observations can be made: i) Data collected in winter and spring (frozen conditions at
 614 surface), presented by blue symbols, show resistivity values higher than those expected from
 615 laboratory measurements, which aligns with the field observations reported by Maierhofer et al
 616 (2024). This may be related to the salt segregation during freezing, which may enhance

617 conductivity of pore water and consequently reduce resistivity of samples. ii) At higher
 618 temperature (unfrozen conditions at surface), a linear trend is observed that aligns with
 619 laboratory measurements for part of datasets (e.g., datasets of 26/08/2020 and 17/09/2020). The
 620 difference in resistivity between field and laboratory data under unfrozen conditions could be
 621 attributed to the heterogeneity at the field scale and/or the difference in water content and water
 622 salinity between laboratory and field environments. Whereas laboratory measurements were
 623 conducted in saturated conditions (saturation was performed under vacuum using degassed
 624 water). iii) Field data exhibit greater dispersion compared to laboratory data, which can be
 625 attributed to several factors, including 3D effects at the site, the influence of infrastructure and
 626 heterogeneity at different scales (from fractures scale to pore scale). In addition, there is a
 627 difference in resolution between the two field measurements: temperature measurements are
 628 local, while resistivity measurements account for a larger volume.



629
 630 **Figure 12.** Resistivity vs. temperature. Resistivities are extracted from the tomograms in Figure D1 at
 631 location P1. Temperature is measured by sensors at BH-NW. Laboratory data on two granite samples
 632 and fitting with Equation 1 and 2 are shown too.

633

634

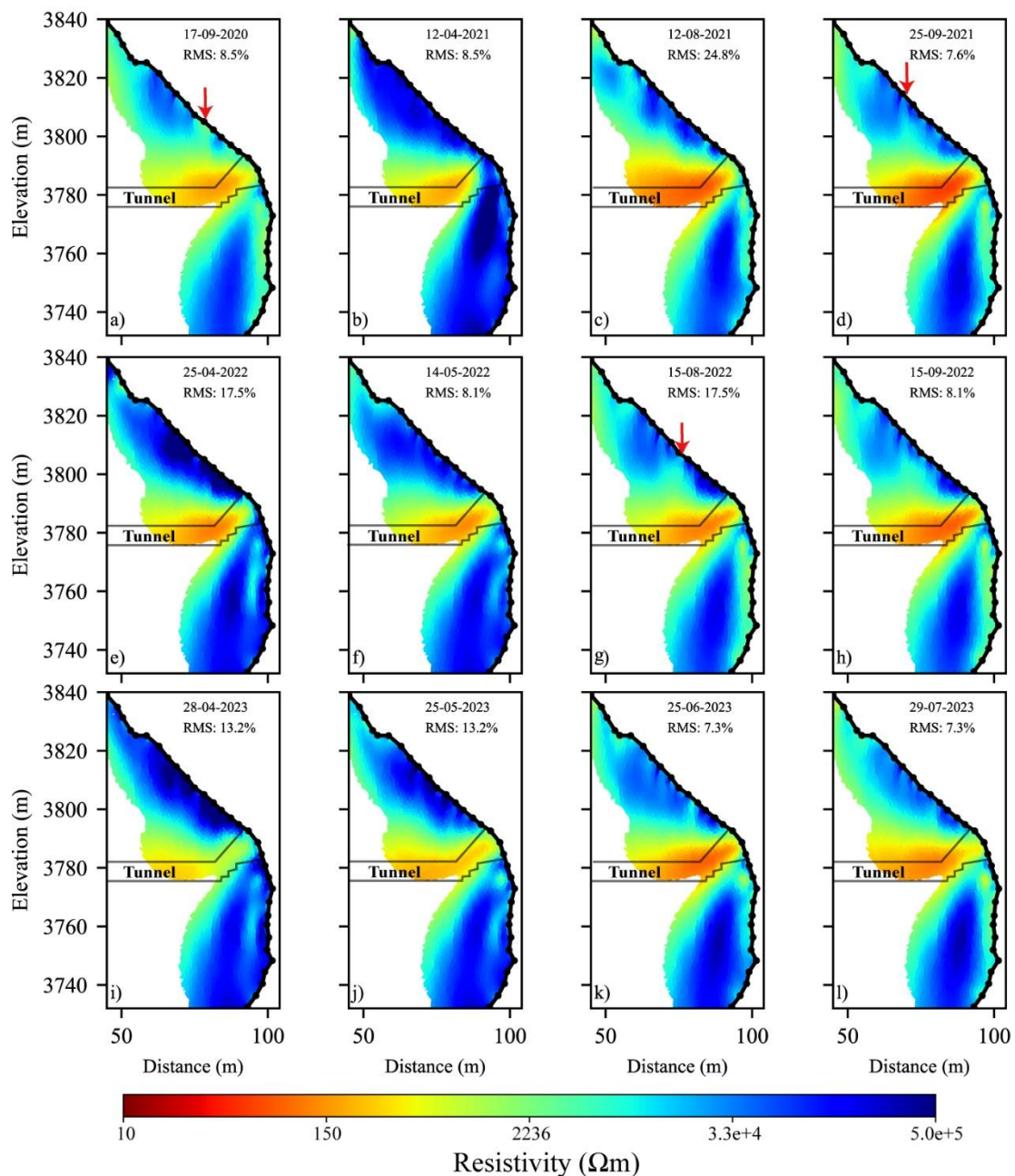
635 **5.65. Hydrogeological dynamics**

636 One of the objectives of this study was to assess hydrogeological dynamics. Due to gaps
637 in the ERT time series, the analysis of times series did not yield conclusive information.
638 Therefore, we selected specific datasets (nearly complete pseudo-sections) and compared the
639 results of the time-lapse inversion to gather information about water infiltration and drainage.
640 Although we could not precisely identify the infiltration and drainage pathways or the water
641 table (which may be located at a lower altitude according to Magnin and Josnin (2021)) using
642 ERT measurements, we observed several instances that serve as evidence of possible water
643 flows.

644 Figure 13 shows the results of the time-lapse inversion of datasets along the S profile at
645 various time intervals. The same inversion parameters were applied as those used to invert the
646 datasets on the NW side (Fig. 78). In the upper part of the profile (*i.e.*, above the gallery), we
647 interpret that seasonal variations in resistivity are influenced by the presence of fractures, which
648 control water flow pathways and, consequently the resistivity response throughout the seasonal
649 cycle. This portion of the profile is exposed to strong insolation in summer, which dries the
650 rock and fractures, leading to an increase in resistivity near the surface due to air-filled pores
651 and fractures (*e.g.*, Fig 13ba, c and l). Conversely, decreases in resistivity in this zone (*e.g.*, Fig
652 13a, d and g), can be attributed to higher water saturation caused by the circulation of snowmelt
653 or rainfall water. Snowmelt on this side supplies substantial amounts of water throughout the
654 thawing season (Ben-Asher et al., 2023). The conductive zone observed beneath the desiccated
655 area (*e.g.*, Fig. 13d and h) likely corresponds to zone of increased water saturation, as also
656 reported by Sass (2004).

657 In the lower part of the S profile (*i.e.*, below the gallery), the seasonal variations in
 658 permafrost resistivity are clearly observed and can be tracked over time, with no evidence of
 659 significant water flow or drainage in this zone. This portion of the S profile shares a similar sun
 660 exposure to the NW profile and therefore exhibits comparable dynamics, with the development
 661 of a thawed and more water saturated active layer than in the upper part, because it is less
 662 exposed to solar radiation, it undergoes less desiccation than the south face sector.

663



664

665 **Figure 13.** Tomograms of resistivity along the south side (S profile). Electrical resistivity tomograms at
 666 different dates (from September-2020 to July-2023). The conductive zone (in warm-colors) explained
 667 by the presence of the gallery. The red arrows indicate the potential zones of water infiltration from
 668 snowmelt or precipitation.

669

670 **6. Discussion**

671 In this study, we use repeated and automated ERT to investigate the evolution of
 672 permafrost at a high altitude rockwall site. As expected, data from A-ERT are of lower quality
 673 compared to manual measurements, where the operator can intervene to improve CR after each
 674 electrode check (Doetsch et al., 2015; Hilbich et al., 2009). ~~The high CR is the main~~ challenge
 675 preventing the year-round collection of high quality data at high altitude rockwall sites such as
 676 the site investigated in this study ~~problem for getting good and durable A-ERT.~~ Therefore,
 677 conducting ERT in frozen surface conditions on rockwall permafrost remains challenging
 678 because of the high CR. Various approaches were tested to improve CR. For instance,
 679 duplicated electrodes provided a durable and significant improvement in CR (~ one order of
 680 magnitude reduction), helping to enhance data quality.

681 Time lapse inversion of the measured resistivity showed the seasonal and interannual
 682 variations (Fig. [78](#), [89](#) and 13). We observe that resistivity decreased over time at greater depths
 683 (e.g., at P1 and P2, comparing data from July 30, 2020, and July 30, 2022), indicating
 684 degradation of the permafrost ~~such~~ as also revealed by borehole measurements (Magnin et al.,
 685 2024). However, this decrease in resistivity is minor, likely due to the relatively short
 686 observation period of two years at NW side and four years at S side. A thicker active layer is
 687 observed at the upper section, which can be attributed to 3D heat transfer processes and the
 688 close proximity of the shaded north-west face to the sun-exposed southern faces in the upper
 689 part of the slope (Magnin et al., 2017; Noetzli et al., 2007).

690 The contrast between the resistivity in the active layer and that in permafrost is not
 691 significant in the lower section on the NW side at BH-NW (P1 Fig. [89](#)), which may result from

692 low ice content/water content where the porosity is around 1 %,the insulating effect of snow
693 accumulated in the zone of the BH-NW or due to high surface conductivity in granite. The
694 alteration of granite involves the transformation of primary minerals (mica and alkali feldspars)
695 into secondary clay minerals (such as kaolinite), which are known for their high cation
696 exchange capacity and, consequently, their contribution to surface conductivity (Piolat et al.,
697 2025; Revil et al., 2024). Additionally, the sensitivity of the used electrode array (with a
698 smallest quadrupole length of 15 m) could affect the resolution of ERT image near the surface
699 (Binley and Kemna, 2005).

700 One of the objectives of this study was to evaluate the potential of using field resistivity
701 measurements to provide 2D or 3D information on thermal distribution in permafrost, based on
702 the superposition of resistivity and temperature datasets. The temperature estimation based on
703 ERT data leads to good agreement with observed temperatures, with a mean absolute error
704 differences of less than ± 1 °C at depths between of 4-2.5 to 10m, indicating that the proposed
705 model (Equation 2) can reasonably reproduce subsurface permafrost temperatures.
706 Consequently, this approach can provide valuable insights into the site's thermal distribution
707 as shown in Figure 11, even though internal permafrost temperatures typically lie just a few
708 degrees below freezing (e.g., Noetzli et al., 2024). However, a precision of ± 1 °C may be
709 insufficient in permafrost studies, where minor temperature variations can greatly impact
710 stability and long-term thermal evolution. Nevertheless, this level of accuracy remains within
711 the uncertainty range commonly reported for thermal models (Magnin et al., 2017).

712 On the other hand, predicting temperature in the active layer remains challenging, as
713 temperature is not the dominant factor affecting resistivity in thawed conditions. Data collected
714 under frozen surface conditions (*i.e.*, measurements taken in winter and spring with high contact
715 resistance) resulted in larger discrepancy between estimated and measured temperature and

716 could not be reliably used for temperature estimation. Consequently A-ERT measurements
717 remain challenging when the ground surface is frozen, mainly due to the high contact resistance.

718 Furthermore, the transition between frozen and unfrozen conditions is not clearly
719 distinguished at resistivity curve extracted from field measurements (see Fig. 89, 10). The
720 freezing point, which is expected to result in a significant change in resistivity (as observed in
721 laboratory measurements), does not exhibit the same effect in field. However, some datasets
722 (e.g., datasets of 12/08/2021 and 17/09/2021) show progressive increase in resistivity when
723 temperature decreased (*i.e.*, indicating progressive freezing). This point needs to be addressed
724 in further research with a smaller electrode array to improve the resolution of geophysical
725 measurements.

726 On the sun exposed face, the tomograms of resistivity show near-surface pore
727 desaturation, attributed to strong insolation on the rock face that is perpendicular to the sun
728 beam, along with features that may relate to water infiltration along fractures. The exact
729 pathways of infiltration and drainage are still ambiguous, possibly due to the resolution of
730 resistivity measurements. With the AdM setting, we can also hypothesize that the saturated
731 conditions are almost never reached. There is water circulation, but no pressurization or
732 development of a water column, because the water table is likely lower than the area covered
733 by the measurements (Magnin and Josnin, 2021), conversely to Offer et al. (2025) at the
734 Kitzsteinhorn for example. Indeed, our investigation is in a different setting: high altitude peak
735 lying ~1000 m above the water table (Magnin and Josnin, 2021) while in the Kitzsteinhorn
736 outcrops from a glaciated areas with a probably much closer water table.

737 Finally, A-ERT acquisition using smaller electrode array can improve near surface
738 resolution and provide more detailed information about the subsurface. Combining ERT with
739 other geophysical methods, such as induced polarization and/or refraction seismic tomography,

740 can also provide complementary petrophysical and spatial sensitivity, enabling a more
741 comprehensive investigation of the hydrogeological system of high mountain permafrost.

742

743 **7. Conclusions**

744 We used repeated and Automated Electrical Resistivity Tomography (A-ERT) to
745 monitor permafrost dynamics over nearly four years at AdM in the French Alps, aiming to
746 better understand the complexities of permafrost behavior in response to climatic variations and
747 to explore the potential of the method for quantitative monitoring. The key findings are
748 summarized as follows:

- 749 1. Through detailed analyses of ERT data, we were able to characterize the active layer
750 dynamics and identify significant seasonal and multiannual changes in permafrost
751 evolution. Importantly, we observed that the ALT and permafrost conditions below
752 varied significantly from one face to another in coherence with climate signals and
753 measured temperatures in boreholes.
- 754 2. This research demonstrates that temperature can be quantitatively derived from
755 geophysical measurements of electrical resistivity based on a petrophysical model
756 connecting resistivity to temperature with precision of approximately ± 1 °C in
757 frozen granite during summer and autumn monitoring.
- 758 3. Our assessments of the hydrogeological system revealed instances of possible water
759 flow as well as bedrock desiccation under strong insolation. That said, the exact
760 pathways of infiltration and drainage remain unclear.
- 761 4. The results underscore the utility of ERT as a promising, non-invasive approach for
762 quantitative monitoring non-linear permafrost evolution in high mountains.

763 Although installation of A-ERT system is relatively low costs, it can requires substantial
764 maintenance in high-risk areas like, especially on unstable high mountain rockwalls where

765 rockfalls and lightning effects ~~can lead to~~ damaging ~~equipment of cable~~. This study highlights
766 the urgent need to address challenges related to climate conditions at high-altitudes that affect
767 device performance and contact resistances, in order to enhance the reliability and durability of
768 continuous A-ERT data collection.

769

770

771

772 **Data availability.** Data will be made available on request to the corresponding author.

773 **Author contributions.** FA performed the data analysis, prepared the figures, and wrote the
774 majority of the text. JB contributed to data acquisition, writing, and figure preparation. FM and
775 AR contributed to the design of the ERT survey, as well as data acquisition and discussion of
776 the results. EM, MBA, LR and PAD contributed to the field installation and acquisition, JR
777 conducted and processed the laboratory data, MK contributed to data inversion and discussion,
778 TC provided air temperature data, PAD offered additional information about the site. Finally,
779 all authors actively contributed to the preparation of this version of the paper.

780

781 **Competing interests.** The authors declare that they have no conflicts of interest.

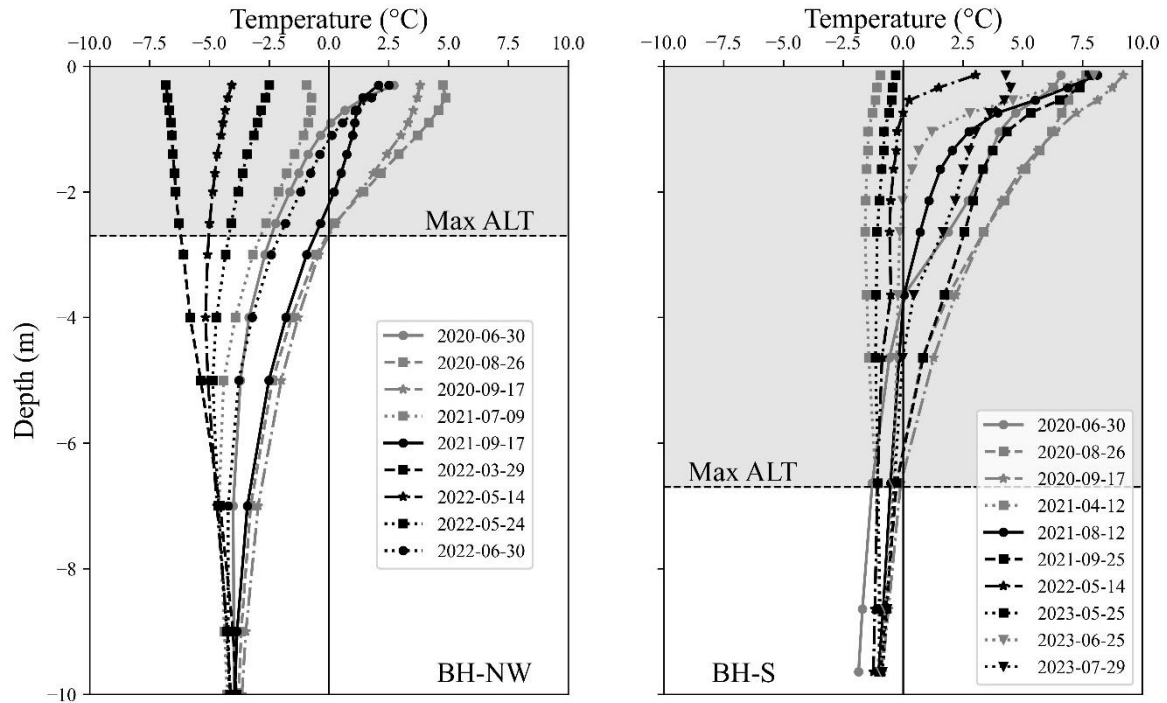
782

783 **Acknowledgments.** This research is part of the ANR WISPER project (ANR-19-CE01-0018)
784 and the Action Plan on Risks from Glacial and Periglacial Origin (PAPROG) from the French
785 Ministry of Ecological Transition, Biodiversity, Forest, Sea and Fishing. The authors
786 acknowledge the following persons who helped with the field work: Antoine Chabas, Bruno
787 Galabertier, Stéphane Jaillet and Raphaël Gallet from the EDYTEM Laboratory, Simon Alesina
788 from the University of Lausanne, Marc Cleriot for help, and Catherine Coulaud from IGE. The
789 authors are also grateful for the Compagnie du Mont-Blanc that provided access to the site and

790 support. Finally, we thank Vincenzo Lapenna and the four anonymous Referees for their
791 constructive reviews, and we are especially grateful to the Editor, Teddi Herring for her
792 valuable comments during the review of this paper.

793 **Appendix A: Temperature measurements in boreholes on different date BH-NW and**

794 **BH-S**

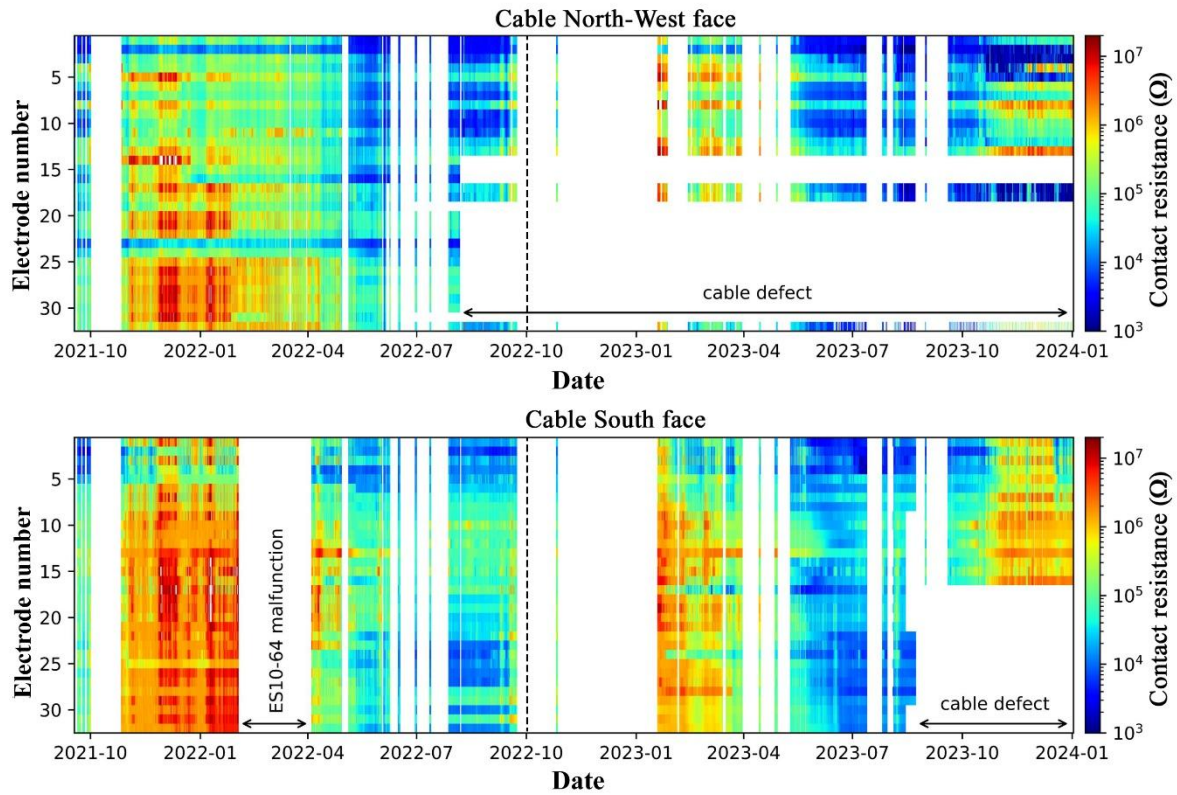


795

796 Figure A1: Temperature variation over depth in boreholes BH-NW and BH-S on different dates
 797 aligned with the ERT measurement periods shown in Figures 7&, 12 and D1. The gray-shaded area
 798 indicates the extent of the active layer at each borehole.

799

800 **Appendix B:** Evolution of the contact resistance (CR) over time at NW and S profiles. The
 801 CR measured before each daily measurement between 09/2021 and 12/2023 are presented in
 802 Figure B1.



803

804 **Figure B1.** Temporal evolution of contact resistance at the North-West side and South side. Data partly
 805 missing is due to cable defects. The vertical dashed line indicates the date at which the duplicate
 806 electrodes were installed. panels highlighted by dotted lines (A1, B1 and C1) are compared with their
 807 corresponding periods (A2, B2, and C2) to evaluate the change in contact resistance after doubling the
 808 electrodes.

809

810

Appendix C: Summary of data presented in this study

811 **Table C1.** Summary of data presented in this study. Number of data before filtering is 155
 812 datum points of Wenner configuration. Most of datasets have more than 80% of total number
 813 of measurements. Two datasets have more than 40% of lost data because of disconnected
 814 electrodes.

815

Date	N-W Profile		S Profile	
	Number of data after filter	Percentage (%)	Number of data after filter	Percentage (%)
30-06-2020	151	97.5	-	-
26-08-2020	149	96.1	90	58
17-09-2020	151	97.5	90	58
12-04-2021	118	76.1	121	78
09-07-2021	114	73.5	-	-
12-08-2021	149	96.1	140	90.3
17-09-2021	145	93.5	131	84.5
25-09-2021	143	92.2	144	92.9
29-03-2022	121	78	-	-
25-04-2022	141	91	131	84.5
14-05-2022	141	91	147	94.8
24-05-2022	140	90.3	146	94.1
30-06-2022	102	65.8	-	-
30-07-2022	-	-	145	93.5
15-08-2022	-	-	145	93.5
15-09-2022	-	-	144	93
19-03-2023	-	-	138	89
28-04-2023	-	-	143	92.2
25-05-2023	-	-	148	95.5
25-06-2023	-	-	144	92.9
29-07-2023	-	-	140	90.3

816

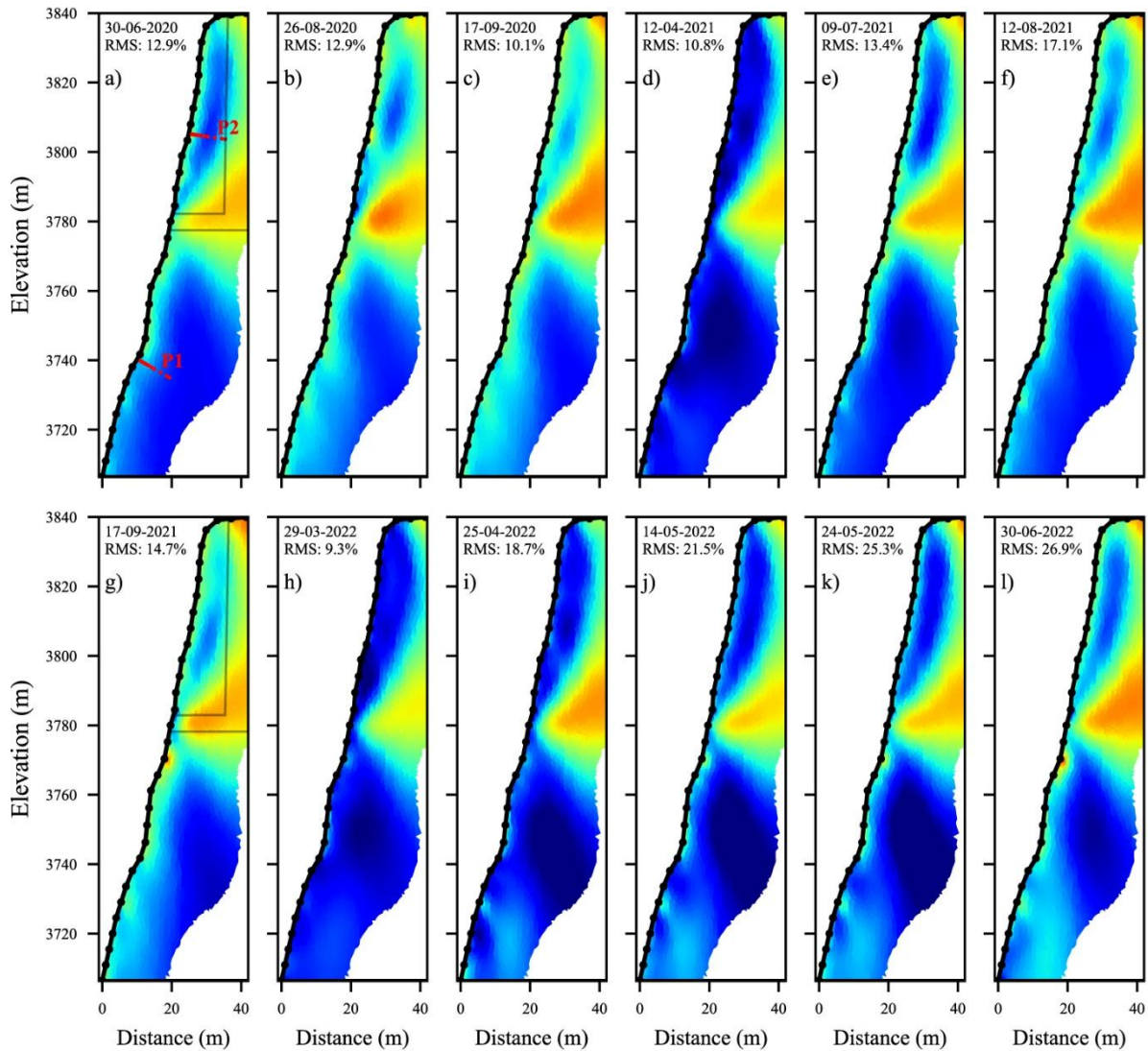
817

Appendix D: Time-lapse inversion results

818 Appendix D presents time-lapse inversions of a large number of datasets from north-west face

819 and south faces. The Resistivity variation ratio between consecutive electrical resistivity

820 tomograms is also evaluated. A summary of these datasets is provided in Table 1C.



821

822 **Figure D1.** Electrical resistivity tomograms at different dates (from June-2020 to June-2022) along the

823 NW side (NW profile). The conductive zone (in warm colors) indicates the approximate position of the

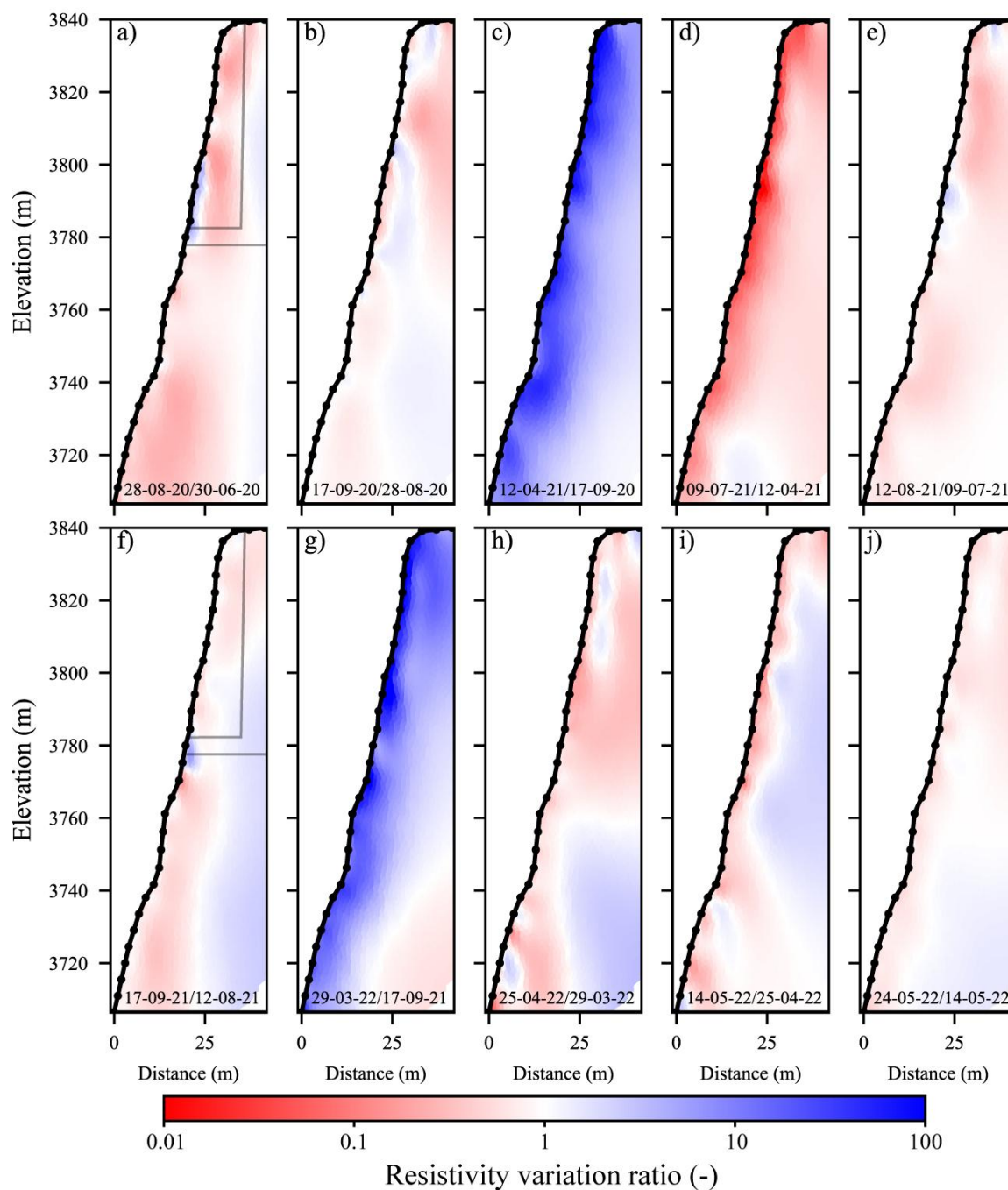
824 gallery and elevator (see Fig. 56). The red dots (P1 in panel a) indicate the positions of the thermal

825 sensors in the borehole BH-NW. Data presented on Figures 98, 10 and 11 are extracted at the position

826 of the red dots (P1 and P2).

827

828



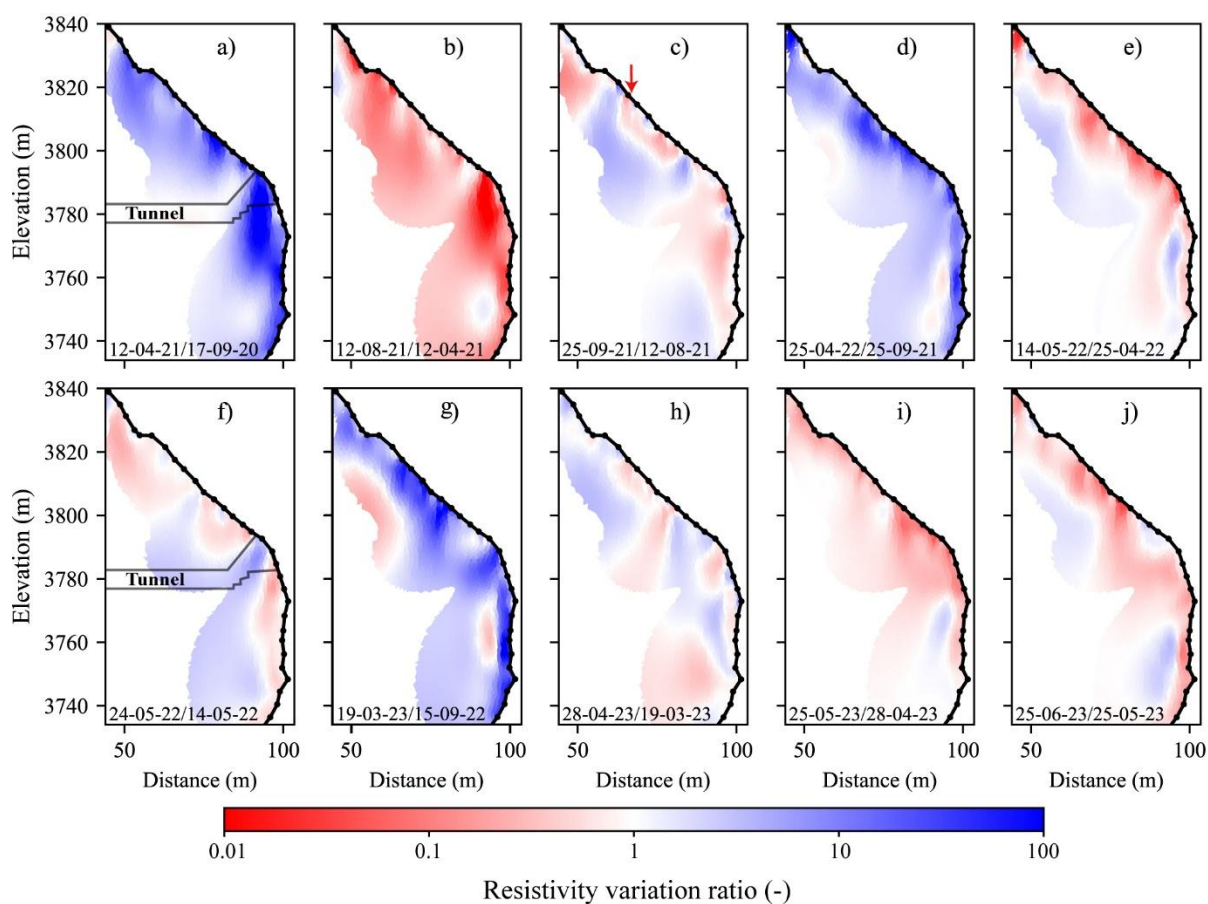
829

830 **Figure D2.** Resistivity variation ratio between consecutive electrical resistivity tomograms (shown in
 831 Fig. 98) along the NW side. Blue colors indicate an increase in resistivity, while red colors represent a
 832 decrease in resistivity from one measurement to the next.

833

834 Figure D2 illustrates the resistivity variation ratio between successive measurements
 835 on the S profile (Figure 1213). The dynamics of the active layer are evident, with freezing-
 836 thawing effects visible near the surface (*e.g.*, Fig. D3a, d, and g). The heat effect (*i.e.*, decrease

837 in resistivity values near the surface) is more pronounced in the lower section (below the
 838 gallery). Another type of anomaly could be observed at greater depth, where heat and/or cool
 839 waves resulting of heat transfer (with delay) lead to local variations at greater depth (*e.g.*, Fig.
 840 D3, e, g and i). In contrast, the fractured zone in the upper portion obscures the temperature
 841 dependency of resistivity due to fluctuations in air and water content (*i.e.*, resistivity in this zone
 842 is impacted by factors beyond just temperature). Water infiltration in this area could explain the
 843 rapid and significant decrease in resistivity observed between 3790 and 3820 m a.s.l. (*e.g.*, Fig.
 844 D3c, f, and j), which increases the thickness of active layer in this zone.



845
 846 Figure D3. Resistivity variation ratio between consecutive electrical resistivity tomograms (shown in
 847 Fig. 13+) along the South side. Blue colors indicate an increase in resistivity, while red colors
 848 represent a decrease in resistivity from one measurement to the next. The red arrow shows the position
 849 of possible water infiltration inferred from the relative variation compared with the surrounding area.
 850

851 **References**

- 852 Abdulsamad, F., Revil, A., Ghorbani, A., Toy, V., Kirilova, M., Coperey, A., Duvillard, P. A., Ménard,
853 G., and Ravel, L.: Complex conductivity of graphitic schists and sandstones. *Journal of*
854 *Geophysical Research: Solid Earth*, 124, 8223–8249. <https://doi.org/10.1029/2019JB017628>, 2019.
- 855 Ben-Asher, M., Chabas, A., Josnin, J.-Y., Bock, J., Malet, E., Poulain, A., Perrette, Y., and Magnin, F.:
856 Water flow timing, quantity, and sources in a fractured high mountain permafrost rock wall,
857 *EGUsphere* [preprint], <https://doi.org/10.5194/egusphere-2025-2450>, 2026.
- 858 Ben-Asher, M., Magnin, F., Westermann, S., Bock, J., Malet, E., Berthet, J., Ravel, L., and Deline,
859 P.: Estimating surface water availability in high mountain rock slopes using a numerical energy
860 balance model, *Earth Surf. Dyn.*, 11, 899–915, <https://doi.org/10.5194/esurf-11-899-2023>, 2023.
- 861 Binley, A. and Kemna, A.: DC Resistivity and Induced Polarization Methods, in: *Hydrogeophysics,*
862 *Water Science and Technology Library book series*, edited by: Rubin, Y. and Hubbard, S.
863 S., volume 50, 129–156, https://doi.org/10.1007/1-4020-3102-5_5, 2005.
- 864 Bruel, R., Arthaud, F., Magnin, F., Napoleoni, R., Van Reeth, C., Augé, V., Sagot, C., Fructus, M.,
865 Birck, C., Choler, P., 2026. Different temperature responses of mountain rockwalls, soils, and lakes
866 to summer heat waves. *Reg Environ Change* 26, 34. <https://doi.org/10.1007/s10113-025-02517-3>
- 867 Campbell, S., Rosa T. Affleck, Sinclair, S.: Ground-penetrating radar studies of permafrost, periglacial,
868 and near-surface geology at McMurdo Station, Antarctica. *Cold Regions Science and Technology*,
869 148, Pages 38–49, <https://doi.org/10.1016/j.coldregions.2017.12.008>, 2018.
- 870 Cathala, M., Bock, J., Abdulsamad, F., Deline, P., Josnin, J.-Y., Ravel, L., Revil, A., Richard, J.,
871 Verroust, F., and Magnin, F.: Assessing the role of permafrost in the preconditioning and triggering
872 factors of the September 2020 Crête des Grangettes rockfall (southern French Alps),
873 *Géomorphologie: relief, processus, environnement*, 30, 3, 171–188, <https://doi.org/10.4000/12yqn>,
874 2024.
- 875 Cimpoiasu, M.O., Kuras, O., Harrison, H., Wilkinson, P. B., Meldrum, P., Chambers, J. E., Liljestrang,
876 D., Oroza, C., Schmidt, S. K., Sommers, P., Vimercati, L., Irons, T. P., Lyu, Z., Solon, A., and

- 877 Bradley, J. A. (2025). High-resolution 4D electrical resistivity tomography and below-ground point
878 sensor monitoring of High Arctic deglaciated sediments capture zero-curtain effects, freeze–thaw
879 transitions, and mid-winter thawing. *The Cryosphere*, 19, 401–421, [https://doi.org/10.5194/tc-19-](https://doi.org/10.5194/tc-19-401-2025)
880 401-2025.
- 881 Coperey, A., Revil, A., Abdulsamad, F., Stutz, B., Duvillard, P.A., and Ravel, L.: Low frequency
882 induced polarization of porous media undergoing freezing: preliminary observations and modeling,
883 *Journal of Geophysical Research: Solid Earth*, 124, doi:10.1029/2018JB017015, 2019.
- 884 Dahlin, T., and Zhou, B.: A numerical comparison of 2D resistivity imaging with 10 electrode arrays,
885 *Geophys. Prospect.*, 52, 379–398. <https://doi.org/10.1111/j.1365-2478.2004.00423.x>, 2004.
- 886 Doetsch, J., Ingeman-Nielsen, T., Christiansen, A. V., Fiandaca, G., Auken, E., and Elberling, B.: Direct
887 current (DC) resistivity and induced polarization (IP) monitoring of active layer dynamics at high
888 temporal resolution, *Cold Reg. Sci. Technol.*, 119, 16–28,
889 <https://doi.org/10.1016/j.coldregions.2015.07.002>, 2015.
- 890 Draebing, D.: Application of refraction seismics in alpine permafrost studies: A review, *Earth-Science*
891 *Reviews*, 155, 136–152, <https://doi.org/10.1016/j.earscirev.2016.02.006>, 2016.
- 892 Duvillard, P. A., Revil, A., Qi, Y., Soueid Ahmed, A., Coperey, A., and Ravel, L.: Three-Dimensional
893 Electrical Conductivity and Induced Polarization Tomography of a Rock Glacier, *J. Geophys. Res.-*
894 *Sol. Ea.*, 123, 9528–9554, <https://doi.org/10.1029/2018JB015965>, 2018.
- 895 Duvillard, P.A., Magnin, F., Revil, A., Legay, A., Ravel, L., Abdulsamad, F., and Coperey, A.:
896 Temperature distribution in a permafrost-affected rock ridge from conductivity and induced
897 polarization tomography, *Geophys. J. Int.*, 225, 1207–1221, <https://doi.org/10.1093/gji/ggaa597>,
898 2021.
- 899 Edwards, S. L.: A modified pseudosection for resistivity and IP. *Geophysics*, 42, 1020–
900 1036, <https://doi.org/10.1190/1.1440762>, 1977.
- 901 Etzelmüller, B., Czekirda, J., Magnin, F., Duvillard, P.-A., Ravel, L., Malet, E., Aspaas, A.,
902 Kristensen, L., Skrede, I., Majala, G. D., Jacobs, B., Leinauer, J., Hauck, C., Hilbich, C., Böhme,
903 M., Hermanns, R., Eriksen, H. Ø., Lauknes, T. R., Krautblatter, M., and Westermann, S.:

- 904 Permafrost in monitored unstable rock slopes in Norway – new insights from temperature and
905 surface velocity measurements, geophysical surveying, and ground temperature modelling, *Earth*
906 *Surf. Dynam.*, 10, 97–129, <https://doi.org/10.5194/esurf-10-97-2022>, 2022.
- 907 Farzamian M, Vieira G, Monteiro Santos FA, et al.: Detailed detection of active layer freeze-thaw
908 dynamics using quasi-continuous electrical resistivity tomography (Deception Island, Antarctica).
909 *Cryosphere*.14(3):1105-1120. <https://doi.org/10.5194/tc-14-1105-2020>, 2020.
- 910 Günther, T., Rücker, C., and Spitzer, K.: Three-dimensional modelling and inversion of dc resistivity
911 data incorporating topography-II. Inversion. *Geophysical Journal International*, Volume 166, Issue
912 2, August 2006, Pages 506–517, <https://doi.org/10.1111/j.1365-246X.2006.03011.x>, 2006.
- 913 Hartmeyer, I., Delleske, R., Keuschnig, M., Krautblatter, M., Lang, A., Schrott, L., and Otto, J.-C.:
914 Current glacier recession causes significant rockfall increase: the immediate paraglacial response
915 of deglaciating cirque walls, *Earth Surf. Dynam.*, 8, 729–751, [https://doi.org/10.5194/esurf-8-729-](https://doi.org/10.5194/esurf-8-729-2020)
916 2020, 2020.
- 917 Hasler, A., Gruber, S., Font, M., and Dubois, A.: Advective Heat Transport in Frozen Rock Clefts:
918 Conceptual Model, Laboratory Experiments and Numerical Simulation, *Permafrost and Periglacial*
919 *Processes*, 22, 378–389, <https://doi.org/10.1002/ppp.737>, 2011.
- 920 Hauck, C., Böttcher, M., and Maurer, H.: A new model for estimating subsurface ice content based on
921 combined electrical and seismic data sets, *The Cryosphere*, 5, 453–468, [https://doi.org/10.5194/tc-](https://doi.org/10.5194/tc-5-453-2011)
922 5-453-2011, 2011.
- 923 Hauck, C., and Hilbich C.: Preconditioning of mountain permafrost towards degradation detected by
924 electrical resistivity. *Environ. Res. Lett.* 19 064010. <https://doi.org/10.1088/1748-9326/ad3c55>,
925 2024.
- 926 Herring, T., Lewkowicz, A. G., Hauck, C., Hilbich, C., Mollaret, C., Oldenborger, G. A., Uhlemann, S.,
927 Farzamian, M., Calmels, F., and Scandroglio, R.: Best practices for using electrical resistivity
928 tomography to investigate permafrost, *Permafrost Periglac.*, 34, 494–512,
929 <https://doi.org/10.1002/ppp.2207>, 2023.

- 930 Hilbich, C., Marescot, L., Hauck, C., Loke, M. H., and Mäusbacher, R.: Applicability of Electrical
931 Resistivity Tomography Monitoring to Coarse Blocky and Ice-rich Permafrost Landforms,
932 Permafrost Periglac., 20, 269–284, <https://doi.org/10.1002/ppp.652>, 2009.
- 933 Hilbich, C., Hauck, C., Hoelzle, M., Scherler, M., Schudel, L., Völksch, I., Vonder Mühl, D., and
934 Mäusbacher, R.: Monitoring Mountain permafrost evolution using electrical resistivity
935 tomography: A 7-year study of seasonal, annual, and long-term variations at Schilthorn, Swiss
936 Alps, *J. Geophys. Res.-Earth*, 113, F01S90, <https://doi.org/10.1029/2007JF000799>, 2008.
- 937 Jacquemart, M., Weber, S., Chiarle, M., Chmiel, M., Cicoira, A., Corona, C., Eckert, N., Gaume, J.,
938 Giacona, F., Hirschberg, J., Kaitna, R., Magnin, F., Mayer, S., Moos, C., van Herwijnen, A., and
939 Stoffel, M.: Detecting the impact of climate change on alpine mass movements in observational
940 records from the European Alps, *Earth-Science Reviews*, 258, 104886,
941 <https://doi.org/10.1016/j.earscirev.2024.104886>, 2024.
- 942 Karaoulis, M., Tsourlos, P., Kim, J., and Revil, A.: 4D time-lapse ERT inversion: introducing combined
943 time and space constraints, *Near Surf. Geophys.*, 12, 25–34, <https://doi.org/10.3997/1873-0604.2013004>, 2013.
- 945 Keuschnig, M., Krautblatter, M., Hartmeyer, I., Fuss, C. and Schrott, L.: Automated electrical resistivity
946 tomography testing for early warning in unstable permafrost rock walls around Alpine
947 infrastructure, *Permafrost Periglac.*, 28, 158–171. <https://doi.org/10.1002/ppp.1916>, 2017.
- 948 Krautblatter, M. and Hauck, C.: Electrical resistivity tomography monitoring of permafrost in solid rock
949 walls, *J. Geophys. Res.*, 112, F02S20, <https://doi.org/10.1029/2006JF000546>, 2007.
- 950 Krautblatter M, Verleysdonk S, Flores-Orozco A., and Kemna A.: Temperature-calibrated imaging of
951 seasonal changes in permafrost rock walls by quantitative electrical resistivity tomography
952 (Zugspitze, German/Austrian Alps). *J. Geophys. Res.*, 115, F02003,
953 <https://doi.org/10.1029/2008JF001209>, 2010.
- 954 Krautblatter, M., Funk, D. and Günzel, F.K.: Why permafrost rocks become unstable: a rock–ice-
955 mechanical model in time and space. *Earth Surf. Process. Landforms*, 38, 876–887.
956 <https://doi.org/10.1002/esp.3374>, 2013.

- 957 Loke, M. H.: Time-lapse resistivity imaging inversion, paper presented at 5th Meeting of the
958 Environmental and Engineering Society European Section, Budapest. 1999.
- 959 Magnin, F., Deline, P., Ravanel, L., Noetzli, J., and Pogliotti, P.: Thermal characteristics of permafrost
960 in the steep alpine rock walls of the Aiguille du Midi (Mont Blanc Massif, 3842 m a.s.l), *The*
961 *Cryosphere*, 9, 109–121, <https://doi.org/10.5194/tc-9-109-2015>, 2015b.
- 962 Magnin, F., Krautblatter, M., Deline, P., Ravanel, L., Malet, E. and Bevington, A.: Determination of
963 warm, sensitive permafrost areas in near-vertical rockwalls and evaluation of distributed models by
964 electrical resistivity tomography, *J. geophys. Res.-Earth*, 120, 745–762,
965 <https://doi.org/10.1002/2014JF003351>, 2015a.
- 966 Magnin, F., Ravanel, L., Bodin, X., Deline, P., Malet, E., Krysiecki, J.-M., et al.: Main results of
967 permafrost monitoring in the French Alps through the PermaFrance network over the period 2010–
968 2022. *Permafrost and Periglacial Processes*, 35(1), 3–23. <https://doi.org/10.1002/ppp.2209>, 2024
- 969 Magnin, F. and Josnin, J.-Y. Water flows in Rock Wall permafrost: a numerical approach coupling
970 hydrological and thermal processes. *Journal of Geophysical Research - Earth Surface*, 126(11),
971 e2021JF006394. <https://doi.org/10.1029/2021JF006394>, 2021.
- 972 Magnin, F., Josnin, J.-Y., Ravanel, L., Pergaud, J., Pohl, B., and Deline, P.: Modelling rock wall
973 permafrost degradation in the Mont Blanc massif from the LIA to the end of the 21st century, *The*
974 *Cryosphere*, 11, 1813–1834, <https://doi.org/10.5194/tc-11-1813-2017>, 2017.
- 975 Maierhofer, T., Flores Orozco, A., Roser, N., Limbrock, J. K., Hilbich, C., Moser, C., Kemna, A., Drigo,
976 E., Morra di Cella, U., and Hauck, C.: Spectral induced polarization imaging to monitor seasonal
977 and annual dynamics of frozen ground at a mountain permafrost site in the Italian Alps, *The*
978 *Cryosphere*, 18, 3383–3414, <https://doi.org/10.5194/tc-18-3383-2024>, 2024.
- 979 Mewes, B., Hilbich, C., Delaloye, R., and Hauck, C.: Resolution capacity of geophysical monitoring
980 regarding permafrost degradation induced by hydrological processes, *The Cryosphere*, 11, 2957–
981 2974, <https://doi.org/10.5194/tc-11-2957-2017>, 2017.
- 982 Mollaret, C., Wagner, F. M., Hilbich, C., Scapozza, C., and Hauck, C.: Petrophysical Joint Inversion
983 Applied to Alpine Permafrost Field Sites to Image Subsurface Ice, Water, Air, and Rock Contents,
984 *Front. Earth Sci.*, 8, 1–25, <https://doi.org/10.3389/feart.2020.00085>, 2020.

- 985 Mollaret, C., Hilbich, C., Pellet, C., Flores-Orozco, A., Delaloye, R., and Hauck, C.: Mountain
986 permafrost degradation documented through a network of permanent electrical resistivity
987 tomography sites, *The Cryosphere*, 13, 2557–2578, <https://doi.org/10.5194/tc-13-2557-2019>, 2019.
- 988 Noetzli J., Gruber S., Kohl T., Salzmann N., Haeberli W.: Three-dimensional distribution and evolution
989 of permafrost temperatures in idealized high-mountain topography. *Journal of Geophysical*
990 *Research: Earth Surface* 112, n/a–n/a. <https://doi.org/10.1029/2006JF000545>, 2007.
- 991 Noetzli, J., Isaksen, K., Barnett, J. et al.: Enhanced warming of European mountain permafrost in the
992 early 21st century. *Nat Commun* 15, 10508. <https://doi.org/10.1038/s41467-024-54831-9>, 2024
- 993 Moser, C., Morra di Cella, U., Hauck, C., and Flores Orozco, A.: Spectral induced polarization survey
994 for the estimation of hydrogeological parameters in an active rock glacier, *The Cryosphere*, 19,
995 143–171, <https://doi.org/10.5194/tc-19-143-2025>, 2025.
- 996 Offer, M., Weber, S., Krautblatter, M., Hartmeyer, I., and Keuschnig, M.: Pressurised water flow in
997 fractured permafrost rocks revealed by borehole temperature, electrical resistivity tomography, and
998 piezometric pressure, *The Cryosphere*, 19, 485–506, <https://doi.org/10.5194/tc-19-485-2025>, 2025.
- 999 Pavoni, M., Boaga, J., Wagner, F. M., Bast, A., Phillips, M.: Characterization of rock glaciers
1000 environments combining structurally-coupled and petrophysically-coupled joint inversions of
1001 electrical resistivity and seismic refraction datasets, *Journal of Applied Geophysics*, 215, 0926-
1002 9851, <https://doi.org/10.1016/j.jappgeo.2023.105097>, 2023.
- 1003 Piolat, L., Revil, A., Richard, J., Ghorbani G., Cosme, P., Géraud, Y., Casotti, C., Vaudelet, P., Diraison,
1004 M., and Favier, A.: Induced polarization of volcanic rocks. 8. The case of intrusive igneous
1005 rocks, *Geophysical Journal International*, Volume 241, Issue 2, Pages 1348
1006 1372, <https://doi.org/10.1093/gji/ggaf102>, 2025.
- 1007 Ravanel, L., Magnin, F. and Deline, P.: Impacts of the 2003 and 2015 summer heatwaves on permafrost-
1008 affected rock-walls in the Mont Blanc massif. *Science of the Total Environment*, 609, 132–143.
1009 <https://doi.org/10.1016/j.scitotenv.2017.07.055>, 2017.
- 1010 Revil, A., Cathles, L. M., Losh, S., & Nunn, J. A.: Electrical conductivity in shaly sands with
1011 geophysical applications. *Journal of Geophysical Research*, 103(B10), 23,925–23,936.
1012 <https://doi.org/10.1029/98JB02125>, 1998.

- 1013 Revil, A., Ghorbani, A., Zhao, X., Mouyeaux, A., Barrère, L., Richard, J., Peyras, L., and Vaudelet, P.
1014 Groundwater flow paths using combined self-potential, electrical resistivity, and induced
1015 polarization signals, *Geophysical Journal International*, 239, 2, 798–
1016 820, <https://doi.org/10.1093/gji/ggae291>, 2024.
- 1017 Revil, A., Coperey, A., Mao, D., Abdulsamad, F., Ghorbani, A., Rossi, M., and Gasquet, D. Induced
1018 polarization response of porous media with metallic particles — Part 8: Influence of temperature
1019 and salinity: *Geophysics*, 83, no. 6, E435–E456, <https://doi.org/10.1190/geo2018-0089.1>, 2018.
- 1020 [Revil A., J. Richard, A. Ghorbani, F. Magnin, P.A. Duvillard, M. Marcer, F. Abdulsamad, T. Ingeman-](#)
1021 [Nielsen, L. Ravanel, C. Lambiel, X. Bodin, H. Cai, X. Hu, and P Vaudelet.: Induced polarization](#)
1022 [as a tool to characterize permafrost 1. Theory and laboratory experiments, *Geophysical Journal*](#)
1023 [International, 244, 1. <https://doi.org/10.1093/gji/ggaf443>, 2026a.](#)
- 1024 [Revil A., P. A. Duvillard, M. Marcer, J. Richard, T. Ingeman-Nielsen, F. Abdulsamad, F. Magnin, B.](#)
1025 [Charonnat, H. Cai, X. Hu, L. Ravanel, and P. Schoeneich: Induced polarization as a tool to](#)
1026 [characterize permafrost. 2. Applications to low and high-porosity environments, *Geophysical*](#)
1027 [journal International, 244, 1. <https://doi.org/10.1093/gji/ggaf464>, 2026b.](#)
- 1028 Rucker, C., Günther, T., and Wagner, F. M.: pyGIMLi: An open-source library for modelling and
1029 inversion in geophysics, *Computers & Geosciences*, 109, 106–123,
1030 <https://doi.org/10.1016/j.cageo.2017.07.011>, 2017.
- 1031 Sass, O.: Rock Moisture Fluctuations During Freeze-thaw Cycles: Preliminary Results from Electrical
1032 Resistivity Measurements, *Polar Geogr.*, 28, 13–31, <https://doi.org/10.1080/789610157>, 2004.
- 1033 Scandroglio, R., Draebing, D., Offer, M., Krautblatter, M.: 4D quantification of alpine permafrost
1034 degradation in steep rock walls using a laboratory-calibrated electrical resistivity tomography
1035 approach, *Near Surface Geophys.*, 19, 241–260, <https://doi.org/10.1002/nsg.12149>, 2021.
- 1036 Smith, S.L., O'Neill, H.B., Isaksen, K. et al. The changing thermal state of permafrost. *Nat Rev Earth*
1037 *Environ* 3, 10–23 (2022). <https://doi.org/10.1038/s43017-021-00240-1>
- 1038 Steiner, M., Wagner, F. M., and Flores Orozco, A.: Improved characterization of alpine permafrost
1039 through structurally constrained inversion of refraction seismic data, *The Cryosphere Discuss*,
1040 <https://doi.org/10.5194/tc-2019-52>, 2019.

- 1041 Steiner, M., Wagner, F. M., Maierhofer, T., Schöner, W., and Flores Orozco, A. Improved estimation
1042 of ice and water contents in alpine permafrost through constrained petrophysical joint inversion:
1043 The Hoher Sonnblick case study," *GEOPHYSICS* 86: WB61-WB75.
1044 <https://doi.org/10.1190/geo2020-0592.1>, 2021.
- 1045 Wagner, F. M., Mollaret, C., Kemna, A., and Hauck, C.: Quantitative imaging of water, ice and air in
1046 permafrost systems through petrophysical joint inversion of seismic refraction and electrical
1047 resistivity data, *Geophys. J. Int.*, 219, 1866–1875, <https://doi.org/10.1093/gji/ggz402>, 2019.
- 1048 Zimmermann, E., Kemna, A., Berwix, J., Glaas, W., Münch, H. M., and Huisman, J. A. A high accuracy
1049 impedance spectrometer for measuring sediments with low polarizability. *Measurement Science*
1050 *and Technology*, 19(10), 105603. <https://doi.org/10.1088/0957-0233/19/10/105603>, 2008.